

Dosimetry Dust: An Ultrasonic Backscatter Implantable Dosimetry Device

Stefanie Garcia



Electrical Engineering and Computer Sciences
University of California at Berkeley

Technical Report No. UCB/EECS-2017-205

<http://www2.eecs.berkeley.edu/Pubs/TechRpts/2017/EECS-2017-205.html>

December 13, 2017

Copyright © 2017, by the author(s).
All rights reserved.

Permission to make digital or hard copies of all or part of this work for personal or classroom use is granted without fee provided that copies are not made or distributed for profit or commercial advantage and that copies bear this notice and the full citation on the first page. To copy otherwise, to republish, to post on servers or to redistribute to lists, requires prior specific permission.

Dosimetry Dust: An Ultrasonic Backscatter Implantable Dosimetry Device

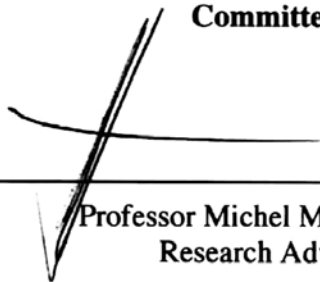
by Stefanie Garcia

Research Project

Submitted to the Department of Electrical Engineering and Computer Sciences, University of California at Berkeley, in partial satisfaction of the requirements for the degree of **Master of Science, Plan II**.

Approval for the Report and Comprehensive Examination:

Committee:



Professor Michel M. Maharbiz
Research Advisor

12/14/2017
(Date)



Professor Kristofer S.J. Pister
Second Reader

12/13/17
(Date)

Dosimetry Dust: An Ultrasonic Backscatter Implantable Dosimetry Device

by

Stefanie Garcia

A report submitted in partial satisfaction of the requirements for the degree

of

Master of Science

in

Electrical Engineering and Computer Science

Committee:

Professor Michel M. Maharbiz, Chair

Professor Kristofer S. J. Pister, Co-Chair

Electrical Engineering and Computer Science

University of California, Berkeley

Fall 2017

Acknowledgments

First and foremost, I would like to thank my advisor **Dr. Michel Maharbiz** for his mentorship, encouragement, and support. When I came to UC Berkeley for graduate school, I was quite lost and unsure of myself and the work I would like to do. I was truly lucky to meet Michel in my first year, after which he provided endless ideas and the guidance which made this project possible.

Next, I would like to thank **Dr. Mekhail Anwar** from UCSF, who provided countless hours of meetings, suggestions, and support for this work. I would also like to thank **Dr. Kavita Mishra** and **Dr. Inder Daftari** from UCSF, who both provided guidance and on-site support at UC Davis's Crocker Nuclear Laboratory. A big thank you as well to the **Crocker Nuclear Laboratory team**. After the extremely long patient treatment days, you all stayed late to help me run these experiments with the beam. For this I am extremely grateful and I am fortunate to have worked with you all.

I would also like to thank **Dr. Kris Pister** for his mentorship, instruction, and encouragement ever since I arrived at UC Berkeley. Kris has always provided me feedback and encouragement in both my professional and personal growth, going above and beyond for all of his students.

I would like to thank the members of the **Maharbiz Lab** for their friendship, guidance, and support. Specifically, I would like to thank **Dongjin (DJ) Seo** and **Konlin Shen** for all of their help in the laboratory in order to make this work possible. Konlin Shen did much of the early wirebonding for me, and his hardware guidance streamlined much of the assembly. I would also like to thank members **Travis Massey**, **Federica Fava**, **Tom Zajdel**, **David Piech**, and **Arda Ozilgen** for their many discussions and feedback that assisted in experimental work.

Lastly, I would like to thank my parents, Petra Mayer-Garcia and Javier Garcia, along with my sisters, Kristina Garcia and Katherine Garcia, for their endless love and encouragement.

Abstract

Proton beam therapy is a well-established medical procedure for treating certain kinds of cancer, and is uniquely suited for treatment of head, neck, and eye tumors. Despite the continuous improvements in medical physics treatment plan simulations, improper tissue irradiation can easily occur if there is a shift in the tumor and/or critical organs during the irradiation process. A fully implantable dosimeter for *in vivo* dose measurements can provide closed loop treatment feedback to a physician during radiation treatments, and assist in enabling full irradiation of a tumor. This work details the theory behind a fully implantable, 1 mm³ MOSFET dosimeter mote, and provides a set of instructions for characterizing this mote for *in vivo* work. An off the shelf nMOS, ALD1106, was irradiated at Crocker Nuclear Laboratory at UC Davis using an ocular melanoma treatment plan. The ALD1106 devices were further characterized with a piezoelectric transducer and a water tank in order to determine backscatter amplitude shifts as a function of dose received, a precursor to future *in vivo* work with an nMOS ASIC. The experimental method used and improvements for the fully implantable device are also described.

Contents

1	Introduction	5
1.1	Motivation	5
1.2	Proton Beam Therapy Methods	7
1.3	Current State of the Art	10
1.4	Thesis Contribution	14
1.5	Thesis Organization	14
2	Wireless Power and Communication	16
2.1	Introduction to Dust	16
2.2	Ultrasonic Power Transfer	17
2.3	Implantable Dosimeter Engineering Strategy	18
2.4	Ultrasonic Backscatter Detection	19
3	MOSFET Radiation Detection and Implantable Strategy	22
3.1	Introduction to MOSFET Radiation Dosimetry	22
3.1.1	Threshold voltage shifts from interface and oxide traps	23
3.1.2	Threshold Voltage, Drain-Source Current, and Transconductance relationships for nMOS	25
4	Experimental Verification	29
4.1	Introduction	29
4.2	Off the Shelf nMOS	29
4.2.1	Experimental Procedure	29
4.2.2	Threshold voltage shift	32
4.2.3	IV Curves	33

4.2.4	Ultrasonic Backscatter Signal	33
5	Conclusions	45
5.1	Future Work - Dosimetry Dust Mote	46
	References	48
	Appendices	52
A	Proton Beam Parameters	53
B	Experimental Code	61
B.1	Data Capture - Ids vs. Vgs	61
B.2	Data Capture - Ids vs. Vds	69
B.3	US Backscatter Integration	75

Chapter 1

Introduction

1.1 Motivation

The primary motivation behind this project is to create a long-term, micro-biomedical implant for *in vivo* dosimetry measurements in radiation oncology applications.

Proton beam therapy is a well-established medical procedure for treating certain kinds of cancer, and is uniquely suited for treatment of head, neck, and eye tumors. In order to effectively treat a patient's tumor, medical physicists have developed various simulations to model proton interactions with tissue and create a patient specific treatment plan that determines optimal gaze angles, the depth of penetration, and width of the spread-out-Bragg Peak necessary to encompass the target tumor. Despite the continuous improvements in medical physics treatment plan simulations, improper tissue irradiation can easily occur if there is a physical shift in the tumor and/or critical organs during the irradiation process (e.g. patient movement). Currently, there are no fully implantable feedback methods to assure proper irradiation of a tumor, and inform a physician what the *in vivo* dose is. We propose the use of a simple MOSFET silicon based radiation detector that employs ultrasonic power harvesting and backscatter communication through the use of a piezoelectric transducer. When a MOSFET is irradiated, there is a characteristic shift in the FET threshold voltage. This shift is primarily due to physical damage in the oxide layer of the device. The change in threshold voltage of the MOSFET is linearly dependent on the amount of oxide damage in the device, and this linear dependence is ideal for stability in our measurements.

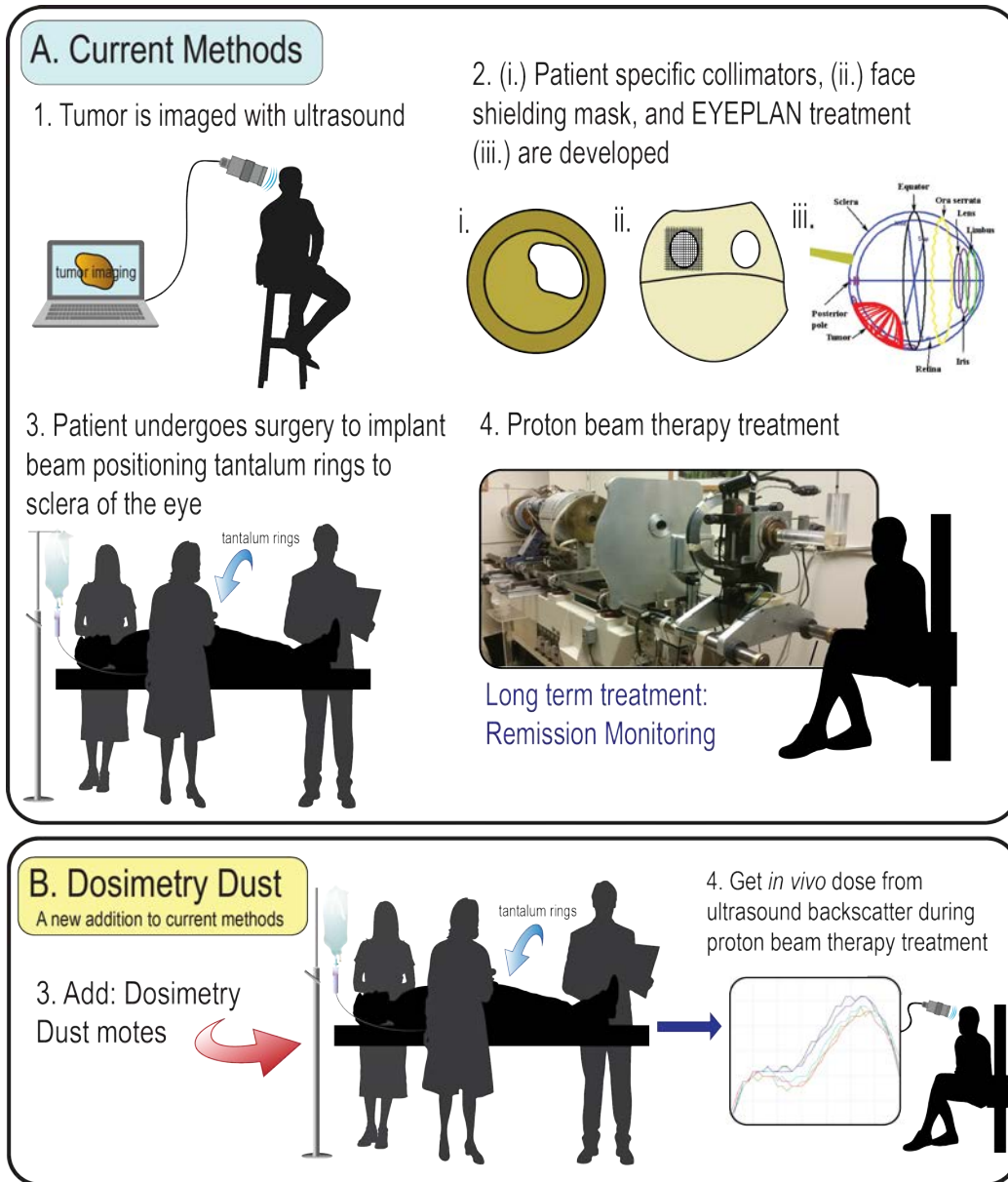


Figure 1.1: A. Outline of current proton beam therapy treatments, and Proton beam therapy treatments starts with ultrasound (US) imaging of the tumor, and develops patient specific materials for the actual radiation treatment. A minimal surgical procedure is required to place 2.5 mm diameter tantalum rings for beam positioning purposes before the proton beam therapy treatment. The EYEPLAN sub-figure in 1.1A, iii. is adapted from [1]. B. Proposed Dosimetry Dust addition to current treatment plan. An implantable dosimeter is added in the surgical step that can provide *in vivo* dosimetry measurements with ultrasound backscatter from the device during proton beam treatments.

To determine localized dose information *in vivo*, we can use radiation induced threshold voltage and I_{DS} shifts to modulate the amplitude of a backscattered ultrasound communication wave, and correlate the received amplitude modulation to a known dose. By implanting these micro Dosimetry Dust devices near the tumor of interest, or near critical organ areas, we can extract important localized dose information.

The current proton beam therapy treatment plan is shown in Figure 1.1A, and further described in the Proton Beam Therapy Methods section. In order to take *in vivo* dosimetry measurements, the ultrasound MOSFET Dosimetry Dust device is proposed to be implanted concurrently with a surgical procedure required for proton beam treatment, shown in Figure 1.1B.

The current ASIC device consists of a dosimeter nMOS, and a resistor bridge (which provides a virtual ground for *in vivo* implants). This is connected to a piezoelectric transducer crystal (PZT) which provides the power and communication capabilities of the finished device.

The Maharbiz and Carmena research groups at UC Berkeley have demonstrated the feasibility of using ultrasonic power harvesting and backscatter communication to wirelessly power and communicate with CMOS implants [2]–[5]. The device has been built and tested for use as an implant in chronic brain machine interfaces [3], [4]. It is possible that the MOSFET in the devices built in [3], [4] can be used as a dosimeter for the proton beam therapies of ocular melanomas done at the Crocker Nuclear Laboratory at UC Davis.

1.2 Proton Beam Therapy Methods

Proton beam therapy is a type of radiation therapy typically reserved for shallow cancers near the surface of the skin. This is due to the physical size of the proton (10^{-15} m), which makes it uniquely qualified for shallow tumor irradiations [6], [7].

Stopping power is the sum of electronic stopping power and nuclear stopping power. For proton interactions in the energy range of interest, nuclear stopping power is negligible (see Figure 1.2) [8]. Electronic stopping power for heavy charged particles (protons, deuterons,

alpha particles) is described by the Blethe - Bloch equation, shown in Equation 1.1.

$$\frac{dE}{dx} = 4\pi r_0^2 z^2 \frac{mc^2}{\beta^2} NZ \left[\ln \left(\frac{2mc^2}{I} \beta^2 \gamma^2 \right) - \beta^2 \right] + \text{corrections} \quad (1.1)$$

$r_0 = 2.818 * 10^{15}m$ is the classical electron radius, z is the charge on the particle, ($z = 1$ for the proton), mc^2 is rest mass of the particle, and Z is the atomic number of the absorber material [9]. Equations describing N , γ , and β are described in Equations 1.2, 1.3, 1.4.

N is the number of atoms/ m^3 in the absorber material,

$$N = \rho(N_A/A) \quad (1.2)$$

where ρ is the density of the absorber material, N_A is Avogadro's number = $6.022 * 10^{23}$, and A is the absorber material's atomic weight.

$$\gamma = \frac{(T + mc^2)}{mc^2} = \frac{1}{\sqrt{1 - \beta^2}} \quad (1.3)$$

T is the particle's incident kinetic energy in MeV.

$$\beta = \sqrt{1 - \frac{1}{\gamma^2}} \quad (1.4)$$

Stopping power typically is shown in units of $MeVcm^2/g$ as a way to normalize it to the density of the material a charged particle is going through (absorber material) . In order to find out how much energy is being deposited in the silicon junction of a MOSFET, one can either use Equation 1.1 to calculate stopping power in silicon, or one can use NIST (National Institute of Standards and Technology) PSTAR which has already done the calculations in Equation 1.1 for a set number of incident energies. In practice, it is suggested that one

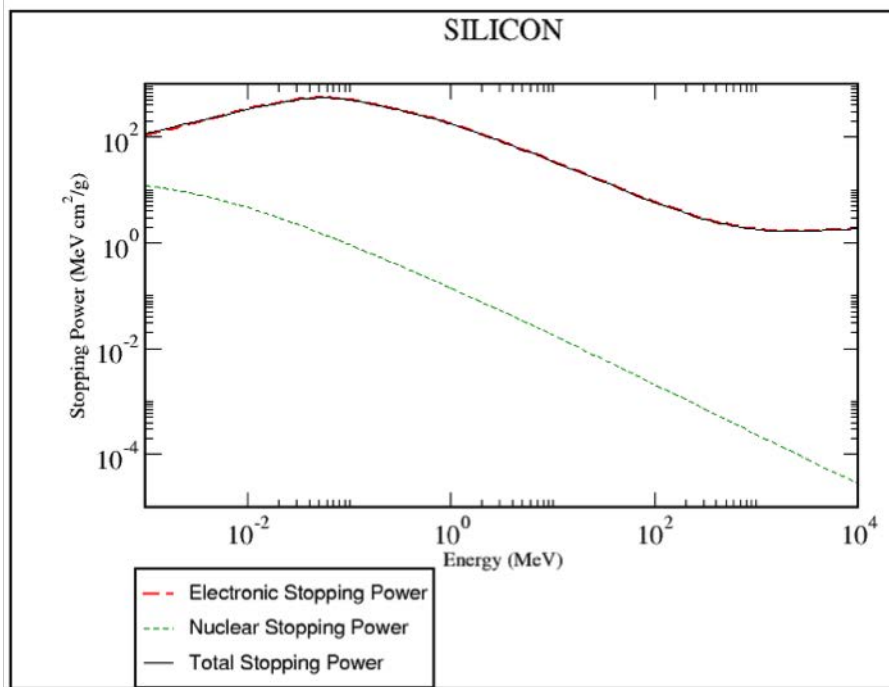


Figure 1.2: Stopping power and ranges for protons in silicon from NIST PSTAR. Data tables of stopping power for incident energy can be downloaded from the NIST website [8]. Note that the nuclear stopping power is negligible for the proton’s stopping power in silicon for the ranges plotted.

download the NIST PSTAR data tables if the incident energy of question is within the NIST range of 10^{-3} to 10^4 MeV. If the energy in question is outside of the range that NIST PSTAR calculates, it is likely that a version of Equation 1.1 will need to be used that includes a mathematical correction for the energy in question [9].

When energy is lost in the absorber material, as described by the stopping power dE/dx , the proton will lose velocity and slow to a stop in the absorber material [10]. A large amount of energy is deposited in the absorber material right before the proton comes to a complete stop, which creates a characteristic peak known as a Bragg Peak. Proton beam therapy utilizes this large dE/dx to deposit large amounts of energy over a small distance, δx , in order to treat shallow tumors effectively. By using multiple bragg peaks together during treatment (so-called Spread Out Bragg Peak, SOBP), a tumor can be irradiated with minimal dose to healthy surrounding tissues [23]. Figure 1.3 A shows a sample proton dose deposition in comparison to electrons and photons, while 1.3 B demonstrates how the proton Bragg

Peak is iterated to create the Spread Out Bragg Peak (SOBP). The SOBP is created using a variable thickness attenuator disk as shown in Figure 1.3 D, which is designed to spread out evenly over a patient's tumor. An example of how the SOBP treats both tumor tissue and the surrounding area for ocular melanoma treatments is shown in Figure 1.3 C.

Figure 1.4 outlines the Crocker Nuclear Laboratory Cyclotron and Proton Beam. The cyclotron utilizes extremely strong magnets to strip an electron off of hydrogen to create a proton. This proton is cyclically accelerated to 67.5 MeV, before entering the treatment room. The primary focus in this work occurs once the proton has entered the treatment room. There are two radiation detectors, the first before a water column, and the second right before the patient collimator, which does raw counts of protons. The water column can be filled to varying water levels to attenuate the beam before the beam reaches the patient. Water column parameters as well as the raw counts for each irradiation are included in Appendix A.

In order to accurately position the proton beam for proton beam therapy, each patient must undergo a surgery prior to scheduled proton beam treatment. In this procedure, tantalum rings with a 2.5 mm diameter are sutured onto the sclera of the eye near the tumor site for beam positioning, shown in Figure 1.5 [6]. The surgery is done 2-3 weeks prior to proton beam treatments in order for swelling to subside from this surgery [6]. This critical step in the current proton beam therapy process provides an opportunity for the Dosimetry Dust implantable device to be attached or sutured into critical dosimetry measurement locations near the tumor, shown in Figure 1.5. A sub-1mm³ Dosimetry Dust device may be attached to the tantalum rings, or implanted into the sclera of the eye itself. The Dosimetry Dust devices will also need to be encapsulated to last the remainder of the patients life (as the tantalum rings are not removed post-treatment), and cause minimal interference with the proton beam treatment.

1.3 Current State of the Art

Although there have been notable advances in miniaturization of CMOS devices for radiation detection [15]–[19], the current state of the art implantable dosimetry continues to use radio

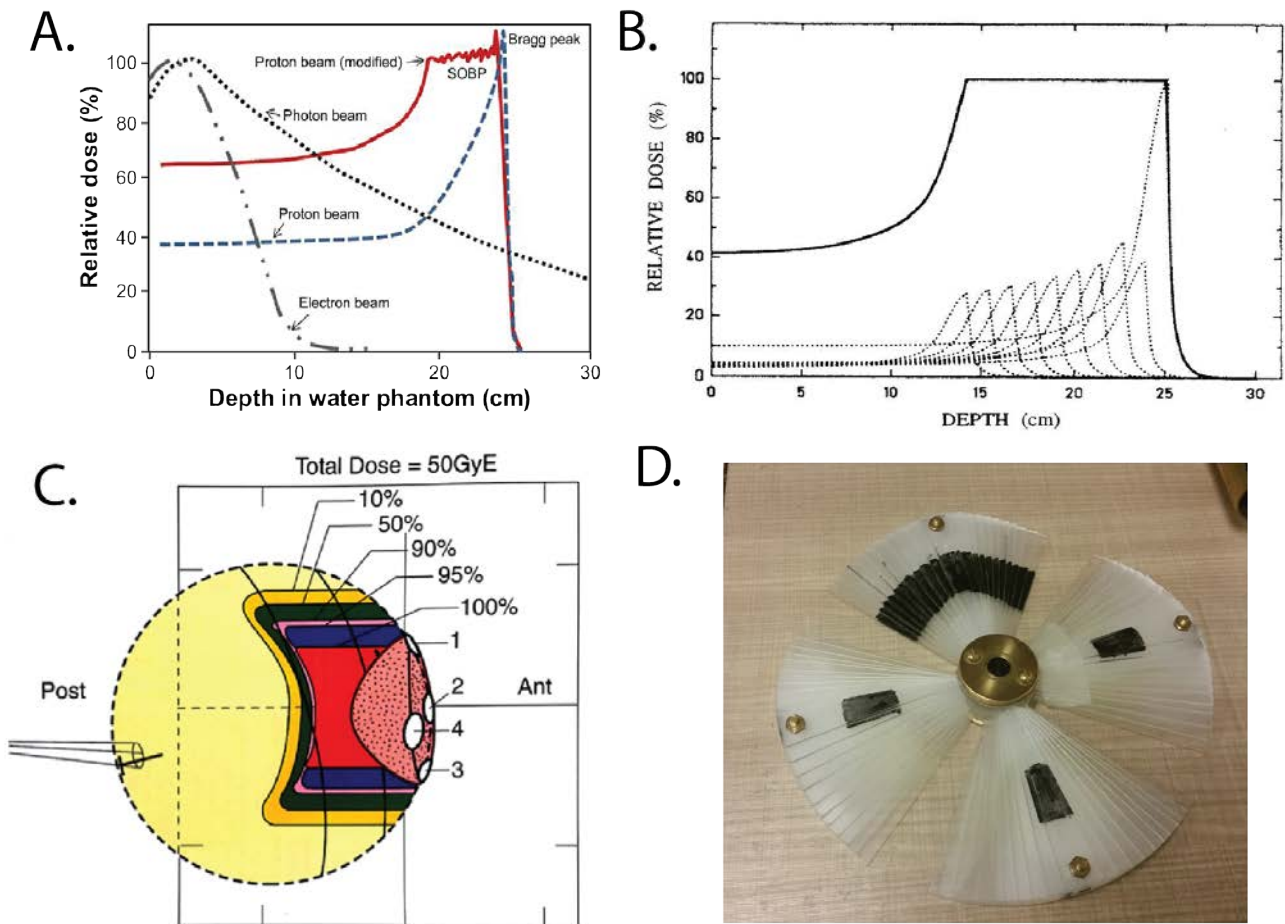


Figure 1.3: A. Bragg peak comparison for photon, electron, and protons, where relative dose is the amount of energy deposited in a mass of absorber material (Dose Depth curves) [11]. B. Spread out bragg peak, adapted from Davino, [12]. C. Patient treatment plan is designed by UC Davis medical physicists designed using EYEPLAN software. Spread Out Bragg Peak (SOBP) calibrations in the beam allow for precise localized tissue irradiation from the EYEPLAN simulations [13] D. Variable thicknesses of a tissue equivalent attenuator are formed into a disk. When spun in the beam path, this attenuator creates a SOBP treatment that is tailored to the patient.

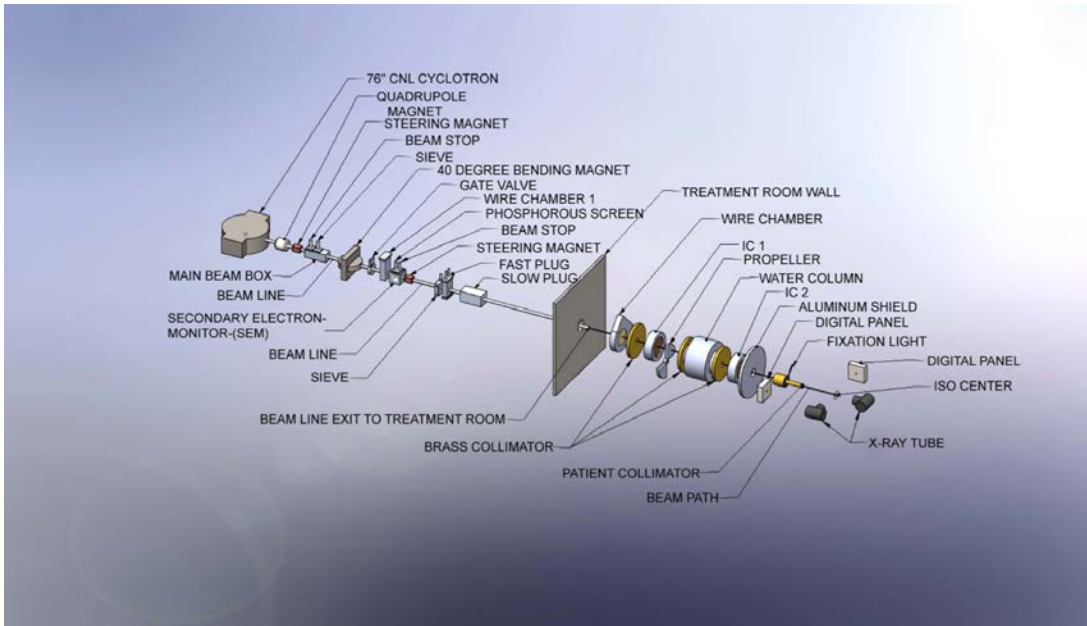


Figure 1.4: Layout of the Crocker Nuclear Laboratory's 67.5 MeV cyclotron and proton beam treatment room. This figure is adapted from [14].

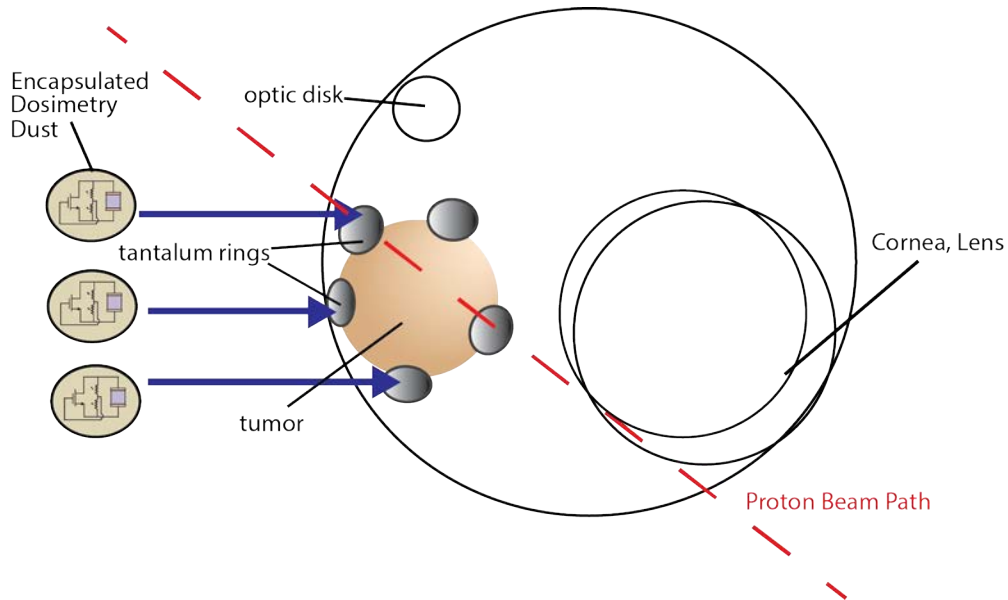


Figure 1.5: Implantation of the Dosimetry Dust device can occur alongside the 2.5 mm diameter tantalum ring implantation surgery. This occurs 2 weeks prior to irradiation [6].

Available Technologies	Maker	Sensor Size	Power/ Communication Platform	Dose Range	Sensitivity
Dose Verification System (DVS)	Sicel Technologies (2011)	2mm x 20mm	RFID	16 Gy	7.8 mV/Gy
MobileMOSFET	Thomson-Nielson/ Best Medical (2016)	0.9mm x 1.1mm x 2.5mm	Physical Reader Box + BlueTooth	Not specified	2.7 mV/cGy
MOSFET Autosense reader	Thomson-Nielson/Best Medical (2016)	a. 1.0mm ² b. 6.25mm ²	Physical Reader Box	a. 70 Gy b. 200 Gy	5μV/cGy
180 nm CMOS dosimeter for wireless In Vivo Dosimetry	Villani E.G. et al 2016	1mm ³	RF	225 Gy	0.6mV/cGy

Table 1.1: There are two main makers that sell on the market implantable dosimeters that utilize the MOSFET as a radiation sensing mechanism; Sicel Technologies and Thomson Nielson Best Medical [20]–[22]. E.G. Vilanni, et al, is also producing a sub-millimeter dosimeter implant with RF technology [15].

frequency (RF) as a communication modality [19].

Limitations in RF technologies must still be investigated when used for implantable radiation detectors *in vivo*, and there still exists a challenge to wirelessly communicate through tissue that must be addressed. There are two main companies that provide MOSFET dosimetry devices to physicians outside of the research phase, Sicel Technologies and Thompson-Nielson Best Medical Canada. Sicel Technologies no longer operates as of 2011, but their Dose Verification System is worth mentioning. The Physical Reader Boxes used by Thomson Nielson Best Medical (Table 1.1), are a wired, *ex vivo* communication platform to the MOSFET dosimeter, which may be placed *in vivo* [21], [22]. Recent research described in [15] shows promising results on miniaturization for RF based radiation devices, but tissue experiments describing RF power harvesting and communication must still be performed to demonstrate feasibility in clinical applications [19]. The novelty of the Dosimetry Dust device is that it will utilize ultrasound (US) as the communication platform instead of RF. It has been proposed that the overall power transmission efficiency in a piezoelectric transducer is higher for ultrasound than RF as receiver size is decreased and positioned farther *in vivo* from the

US interrogator. [23]. This indicates that we have better energy harvesting *in vivo* for an ultrasound-based device, allowing us to have deeper depth of device penetration in tissue and a larger backscattered signal than the RF device alternatives [23].

One final aspect of the Dosimetry Dust device is the aggressive miniaturization of the piezo backscatter communication in the device. Although many current CMOS fabricated devices are on the order of microns, the current size of a radiation detecting ASIC plus RF communication components is a $1 \times 1\text{mm}^2$ device as of 2016 [15]. This device has the potential to be scaled to hundreds to tens of microns [4], [5], allowing for extremely non-invasive, long-term implantable devices.

1.4 Thesis Contribution

This thesis goes through theory, engineering strategies, and experimental steps for the creation of implantable dosimetry devices that use ultrasound for power and communication. Off the shelf devices were first tested at the proton beam at UC Davis's Crocker Nuclear Laboratory, and these were also characterized for ultrasound response. The Neural Dust devices described in [3]–[5] were then taken to the proton beam at Crocker Nuclear Laboratory for initial radiation dose response characterization. Both the successes and failures of these experiments will be described in this thesis to inform future work in this area.

1.5 Thesis Organization

The remainder of this thesis will focus on the two main components of the implantable dosimeter,

1. Theory and design of the ultrasonic wireless power transfer and backscatter communication
2. Theory and design of MOSFET radiation detectors

The wireless power transfer and backscatter communication will be covered in Chapter 2. This will not be covered extensively, however, as the theory is already extensively covered in

[2]–[4]. Chapter 2 primarily focuses on the impedance component of backscatter communication, seeing as this is a key component of the implantable radiation sensing device.

Chapter 3 will extensively cover MOS radiation dosimetry in theory, and introduce the engineering strategy for recovering information about dose in an *in vivo* device. The experimental procedure and results will be covered in Chapter 4, while the conclusions and suggestions for future work will be covered in Chapter 5.

The Appendix will provide further information covering the proton beam parameters used (Appendix A), as well as code used for data collection (Appendix B)

Chapter 2

Wireless Power and Communication

2.1 Introduction to Dust

Smart dust projects began in the late 1990s by the Pister, Kahn, and Boser groups at UC Berkeley. The smart dust project aimed to create autonomous networks of MEMS sensing, communication, and computing motes for a variety of wireless purposes [24]. In 2002, a 16mm^3 solar powered device was demonstrated, which incorporated a $0.25\mu\text{m}$ CMOS ASIC, a 2.6mm SOI solar cell array, and bi-directional optical communication [25]. The original system aimed to scale these sensing devices into a cubic millimeter mote, for use in a variety of defense, agriculture, inventory control, product quality, and environmental applications with optical and/or RF communication [24], [26].

Medical applications of dust started with the Neural Dust project [2]–[5], developed by the Maharbiz and Carmena labs at UC Berkeley. This project sought to develop a neural interface device for long term implantation in order to create a closed loop nervous system interface capable of real time neural recording. A cubic piezoelectric transducer is resonated with ultrasound to provide energy harvesting in the device and backscatter communication. The piezo achieves power harvesting by turning acoustic energy into mechanical energy [3], [4], powering the device *in vivo*. A 60nm ASIC was designed in TSMC, which incorporates a nMOS MOSFET with a symmetric resistor bridge to act as an *in vivo* ground reference.

The devices in Figure 2.1 are the 60 nm Neural Dust ASIC described in [2,3], and were built with the manufacturing process described extensively by Shen, in "Assembly of a Wireless

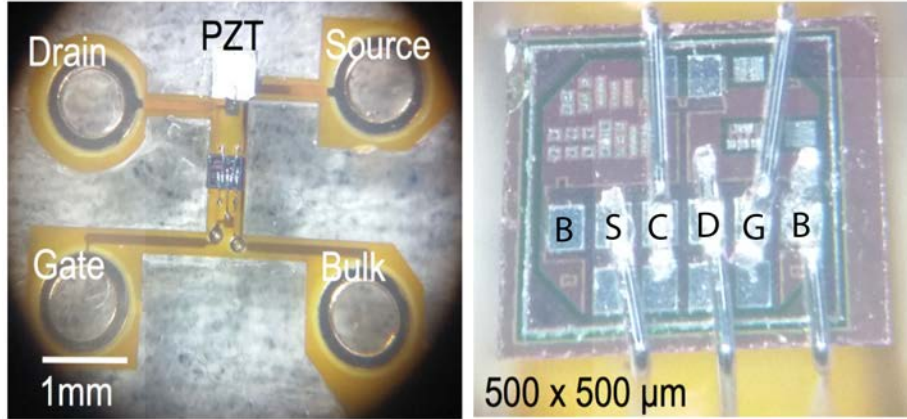


Figure 2.1: A. Fully assembled device with a $750 \times 750 \times 750 \mu m^3$ PZT crystal and ASIC fabricated in a 60nm TSMC process B. Zoom of the $500m \times 500m$ with drain (D), source (S), gate (G), and bulk (B) breakout pads labeled.

Ultrasonic Backscatter System” [5].

2.2 Ultrasonic Power Transfer

Power transfer is highly dependent on the piezo’s orientation relative to the transducer [3], [4]. The power harvesting step of the piezo is critical in getting the maximum backscatter shifts in amplitude. Figure 2.2 shows a figure of the oscilloscope labelling power harvesting and backscatter areas of interest.

In Figure 2.2, a square pulse sequence of 6 pulses at 1.85MHz with an amplitude of $\pm 20V$ is the input pulse at the transducer (yellow curve). Figure 2.2 B shows the power harvested by the piezo as a result of the input pulse (green curve), while Figure 2.2 C is the backscatter amplitude pulse (blue curve) of interest for Chapter 4’s data collection. Power harvesting (green) was done visually for this work, by moving the piezo in 2D until the amplitude of the green power harvesting curve was at a maximum. Once the maximum power harvesting location was determined, the piezo was no longer moved, and extra care was taken to reduce vibrational movement through accidental movement of the water tank.

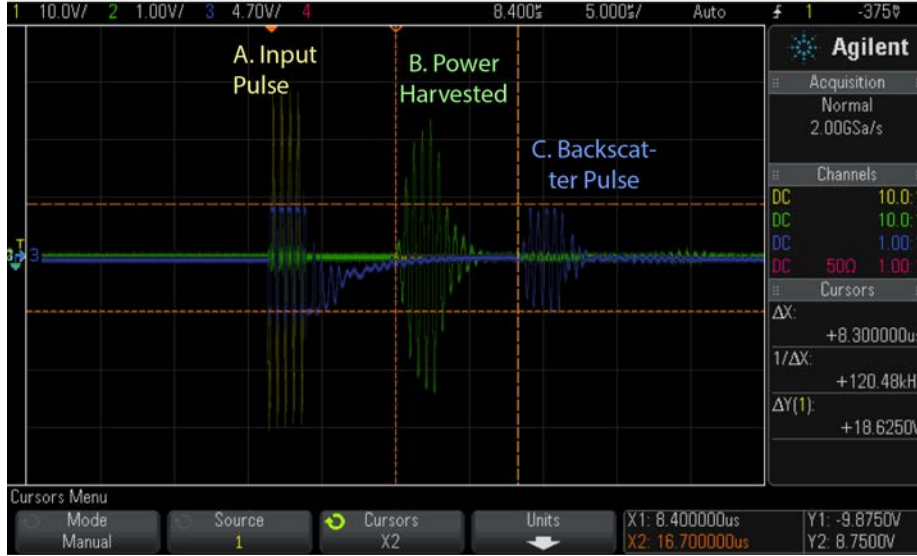


Figure 2.2: A. Example of the transducer input pulse (yellow), B. Power harvesting (green), C. and Backscatter pulse (blue). Maximizing the Power harvesting was done visually by using the oscilloscope to maximize power harvesting pulses (green).

2.3 Implantable Dosimeter Engineering Strategy

The following strategy can be used to correlate radiation dose to the change in threshold voltage, as well as the change in amplitude in the ultrasound backscatter pulse.

1. Irradiate the device with radiation of a known dose in [J/kg]
2. Measure the threshold voltage change in the device δV_T
3. A lower V_T changes the drain-source current drawn for a given V_{DS} , and will also vary impedance seen across the MOSFET's drain to source terminals
4. Change in electrical impedance across the MOSFET modulates the reflection coefficient of the piezo, affecting ultrasound backscatter amplitude

By correlating the US backscatter amplitude to a known radiation dose, a function can be developed that determines an unknown dose *in vivo*.

For the work done in this thesis, the bulk of the MOSFET is tied to a ground port to perform initial dose characterization without a fluctuating AC bulk voltage. For a fully implantable

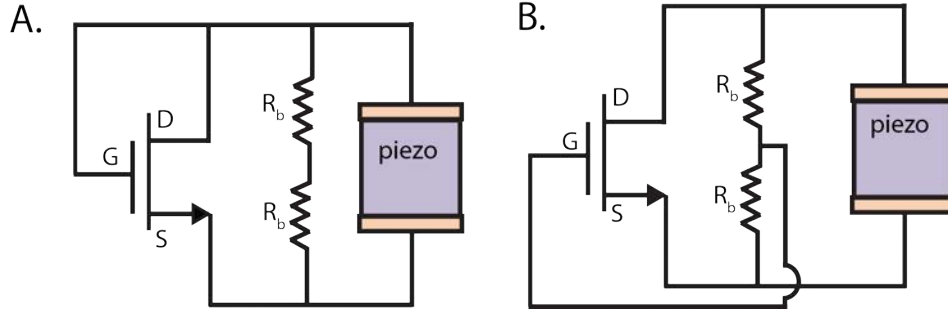


Figure 2.3: The piezo supplies $\pm 1V$ max for a piezo used with a size of $750 \times 750 \times 750 \mu m^3$. A. The drain and gate are tied together in the FET, allowing for measurements in the FET every half cycle of the piezoelectric transducers oscillation (the FET is on for only half of the interrogation cycle). B. This is a symmetric circuit, which allows measurements every cycle (the FET is always on, since I_{ds} constantly switches direction). The maximum V_{gs} will halve the maximum V_{gs} obtained in Figure 2.2 A since the gate is now tied to a symmetric voltage divider.

device, the two circuits diagrams in Figure 2.3 are theoretically proposed, but yet investigated experimentally.

In each of the schematics in 2.3, the bulk is tied to the resistor bridge to allow for an implantable "reference ground" for *in vivo* measurements. The expected effects from this reference ground in regards to it's effect on an implantable dosimeter is further investigated in theory within this work, but not yet measured experimentally. Figure 2.3A ties the Gate and Drain terminals of the nMOS together to make a device that will be turned on every half period, when $V_{gs} > V_t$, and when the V_{gs} is positive. Figure 2.3B ties the gate to the reference ground. Since the nMOS is a symmetric device, the device will always be on when $V_{gs/gd} > V_t$. I_{ds} will switch directions as the gate voltage swings between positive and negative.

2.4 Ultrasonic Backscatter Detection

When more I_{ds} current flows, the impedance seen across the piezo increases. This modulates impedance across piezo, and this impedance seen across the piezo modulates the backscatter signal. In Figure 2.4, the piezo's backscatter pulse is shown. An open across the piezo is

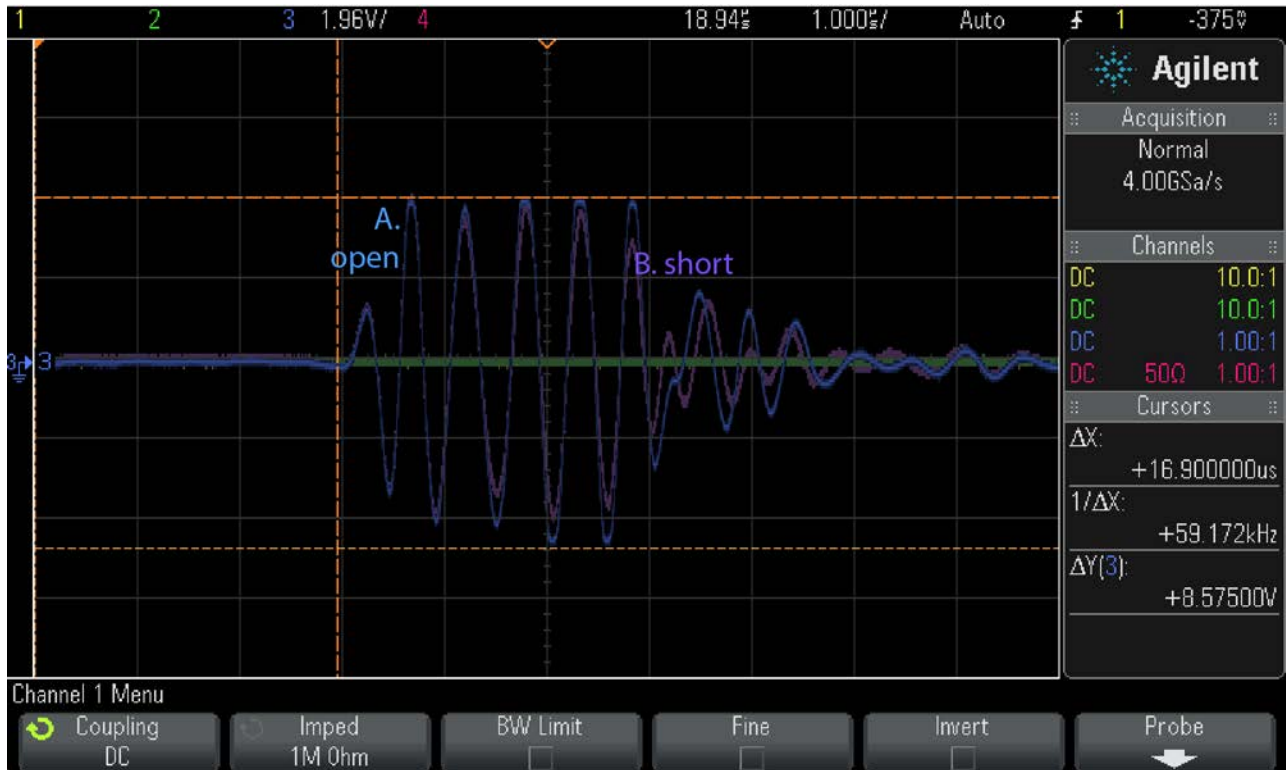


Figure 2.4: Backscatter amplitude when the piezo is open (blue) vs. shorted (purple). More current flow across the piezo when shorted corresponds to a decrease in the backscatter amplitude shift.

shown in curve 2.4 A (blue), while shorting the piezo results in curve 2.4 B (purple). There is a decrease in amplitude of this backscatter signal when the piezo is shorted and current flows.

The piezoelectric transducer currently being used in the device is a PZT (lead zirconate titanate) crystal, however, other piezoelectric materials may also be used. Barium titanate (BaTiO_3) is a good alternative for an implantable piezoelectric transducer, since it does not have any lead in it. For this work, the PZT crystal was selected since it provided a large amplitude shift.

Variations in impedance across the piezo from current flow will be reflected as a change in amplitude in the backscattered US pulse. The relationship of the backscatter amplitude seen at the ultrasound transducer in relation to the impedance across the piezo and impedance losses in tissue is shown in 2.1.

Z_mote % decrease	Reflected Amplitude %	$\Delta\%$ (measured change in amplitude from 0 impedance change across mote)
0%	83.04%	0%
5%	82.23%	0.81%
10%	81.34%	1.70%
15%	80.36%	2.68%
20%	79.26%	3.78%
25%	78.04%	5.00%
30%	76.67%	6.37%
35%	75.11%	7.93%
40%	73.34%	9.70%
45%	71.29%	11.75%
50%	68.90%	14.14%

Table 2.1: Table of Amplitude Shifts using Equation 2.1. Average acoustic impedance in tissue is 1.63×10^6 kg/m³ m/s [27]. Larger tissue impedances will result in larger amplitude shifts for a given I_{ds}

$$Amplitude \propto \left(\frac{Z_{tissue} - Z_{mote}}{Z_{tissue} + Z_{mote}} \right)^2 \quad (2.1)$$

Using Equation 2.1, we can see that nominal mote reflectivity *in vivo* as a percentage of the original pulse gives us a maximum of 83% of the original wave’s amplitude reflected back to the transducer. By varying the impedance seen across Z_{mote} , we can calculate the maximum expected mote reflectivity. For example, if the impedance seen across the mote, Z_{mote} , decreases by 10%, the amplitude seen at the transducer decreases to 81% of the outgoing wave. Table 2.1 some examples of expected amplitude backscatter for a given impedance change as a percentage of nominal.

Chapter 3

MOSFET Radiation Detection and Implantable Strategy

3.1 Introduction to MOSFET Radiation Dosimetry

Radiation induced effects in CMOS devices has been thoroughly investigated and studied over the past several decades [9], [28]. Many initial efforts in radiation characterization arose from the early telecommunications efforts in the late 1950s and early 1960s. In order to develop radiation hardened devices, a detailed understanding of how radiation interacts with CMOS devices was required [29]. Ever since, there have been many efforts in using MOSFETs for dosimetry purposes, in both many areas of modern radiation oncology as well as for in-space dosimetry monitoring in telecommunication satellites [9], [29], [30]. The use of MOSFETs in dosimetry by itself is not novel, and only a brief overview of the relevant physical mechanisms involved in MOSFET dosimetry is further described.

When radiation damage done in the nMOS insulating SiO₂ layer, the threshold voltage needed to turn on the device is lowered linearly to the amount of radiation recieved [17], [28], [31]–[33]. The amount of current generated at a specific V_{gs} bias voltage increases [17], [28], [31]–[33].

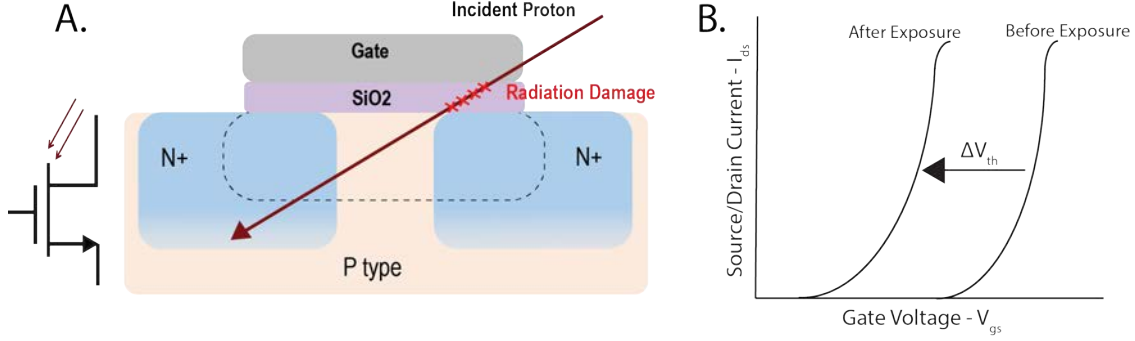


Figure 3.1: A. The nMOS junction. When hit by radiation (a proton is demonstrated by the dark red trajectory line), damage is done in the silicon dioxide SiO_2 junction, which affects the threshold voltage of the device. For an nMOS, the threshold voltage needed at the gate of the nMOS should decrease due to the irradiation damage in the SiO_2 layer.

3.1.1 Threshold voltage shifts from interface and oxide traps

When radiation of any kind hits the MOSFET device, energy is deposited in the device in the form of a dose. We will describe dose using the unit of gray (Gy), which is a unit describing the energy deposited in a material per mass of the material (Joules per Kilogram). Previous research focuses on utilizing the MOSFET as a dosimeter by detecting changes in threshold voltage of the MOSFET [17], [31]–[33]. This requires a measurement of the threshold voltage of the nMOS or pMOS device before radiation, and a subsequent measurement of the threshold voltage post radiation. Radiation damage creates extra holes in the form of $\text{SiO}_2 \equiv \text{Si}\bullet$ and $\text{Si}_3 \equiv \text{Si}\bullet$ Figure 3.1A shows how the insulating SiO_2 is damaged from radiation. In general, nMOS and pMOS devices will both have a negative shift in the threshold voltage required to turn the device on (Figure 3.1B).

There are many theories about the physical mechanism behind this threshold voltage change in the MOSFET when it is exposed to radiation. However, the overwhelming favorite is radiation-induced oxide damage [5]. When ionizing radiation of any sort interacts with the device, the gate oxide of the device (SiO_2) is damaged. This damage is in three forms, 1. Oxide charge, 2. Neutral Traps, and 3. Interface Traps. Only oxide charge and interface traps contribute to threshold voltage shifts from radiation [28].

Oxide charge is created when ionizing radiation generates EHPs in the oxide by physically

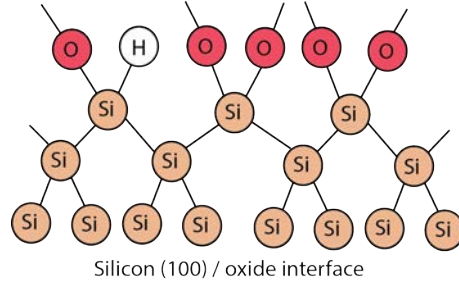


Figure 3.2: (100) interface between the silicon substrate and silicon dioxide (SiO₂)

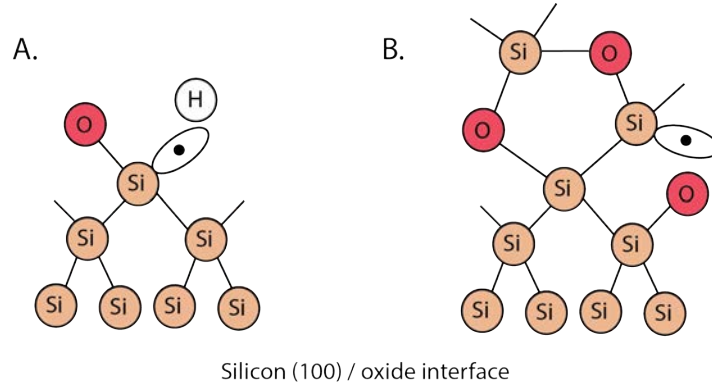


Figure 3.3: When ionizing radiation of any sort interacts with the device, the gate oxide of the device (SiO₂) and the oxide-substrate interface is damaged. This damage creates two main variations of damage: A. Oxide charge B. Interface Traps

breaking bonds between silicon and Oxygen (Si-O). The following model correlates the radiation induced oxide charge, $N_{\text{oxide traps}}$, to the threshold voltage shift and the oxide capacitance [28].

$$N_{ot} = \Delta V_T C_{ox} q^{-1} \quad (3.1)$$

The second contributor to threshold voltage shifts are interface traps, which are generated at the interface between the oxide layer and the substrate. Ionizing radiation here breaks one of silicon-x bonds (where x can be Si, O, or H) a dangling bond in Si is formed. The trivalent bonded Si has one unpaired hole at the interface, which then subsequently affects what threshold voltage is required to turn the MOS device on.

The non-irradiated (100) Si-SiO₂ interface is shown in Figure 3.2. Figure 3.3 shows examples of interface and oxide traps in (100) silicon. Figure 3.3 A shows an interface trap caused by

the Si - H bond being broken, while Figure 3.3 B shows an oxide trap caused by a Si - O bond being broken. These types of bonds break when the device undergoes irradiation, and is a physical mechanism caused by the energy lost in the material when a charged particle travels through it [28].

Device performance in the MOSFET dosimeter is heavily based on the fabrication process, and is particularly dependent on the thermal oxidation step in the CMOS process. In general, thicker oxide layers allow for a larger range of allowed accumulated dose [9], [28]. More defects at the Si-SiO₂ interface, and in the SiO₂ (typically a H-Si bond due to residual hydrogen during thermal oxidation), creates a device that is more sensitive to radiation. The opposite is true as well, if one desires a device that is less sensitive to radiation. Radiation hardening focuses on minimizing Si surface defects, and uses special techniques to dope SiO₂, create pure SiO₂ films, and create double layer oxide structures. There is a linear dependance between the thickness of the oxide layer and the dose range of the MOSFET. As the number of defects in the SiO₂ layer increases, the sensitivity of the device decreases [28].

Total damage of the oxide layer includes trapped charge (oxide charge) and interface traps caused by irradiation [28]. This radiation damage is proportional to the total dose received. In general, a linear function is fit to the MOSFETs change in threshold voltage response (ΔV_t) as a response to the dose received by the device [17], [28], [31], [32]. The fact that this relationship is linear for the dose sensitive region of the device is ideal for stable measurements for the *in vivo* device. Although the change in threshold voltage is the quantifiable effect that describes dose, we must back calculate what this ΔV_t is for any *in vivo* measurements any device will make.

3.1.2 Threshold Voltage, Drain-Source Current, and Transconductance relationships for nMOS

Relevant parameters for an nMOS Transistor are listed in equations 3.2 to 3.7.

$$I_{DS} = \mu_n C_{ox} \frac{W}{L} \left[(V_{GS} - V_T) V_{DS} - \frac{(V_{DS})^2}{2} \right] (1 + \gamma V_{DS}) \quad (3.2)$$

$$I_{DS} = \frac{1}{2} \mu_n C_{ox} \frac{W}{L} (V_{GS} - V_T)^2 (1 + \gamma V_{DS}) \quad (3.3)$$

Eq. 3.2 lists the I_{ds} current in the linear region, while Eq. 3.3 lists the I_{ds} current in the saturation region [34]. Both the active and saturation region currents are considered in this work. The linear region (Eq. 3.2) of the nMOS has a linear relationship with changes in V_t , due to the $(V_{gs} - V_t)$ term. In the saturation region (Eq. 3.3) the threshold voltage has a squared relationship to I_{ds} through the $(V_{gs} - V_t)^2$ term. Theory suggests that for a given V_{gs} , I_{ds} current will increase more when V_t decreases from radiation treatment. This is due to the squared $(V_{gs} - V_t)$ term in the saturation region versus the linear $(V_{gs} - V_t)$ in the linear region. This theory is utilized in the experimental results section of Chapter 4, where the saturation region is used to measure backscatter amplitude in US testing because of this increased change in I_{ds} current in this region.

$$V_T = V_{T0} + \gamma[\sqrt{2\phi_f + V_{sb}} - \sqrt{2\phi_f}] \quad (3.4)$$

$$\gamma = \frac{1}{C_{ox}} \sqrt{2q\epsilon N_A} \quad (3.5)$$

Threshold voltage is described in Eq. 3.4, with the threshold voltage parameter described in Eq. 3.5 [34]. Relevant shifts in threshold voltage due to the radiation is dependant on shifts in both C_{ox} and Fermi level ϕ_f [28].

The transconductance across the nMOS determines what the change in impedance is in the piezo, which corresponds to the amplitude backscatter. Transconductance is the inverse of resistance, and is described by equations 3.6 and 3.6 for an nMOS.

The top-gate transconductance is described by Equation 3.6.

$$g_m = \mu C_{ox} \frac{W}{L} (V_{GS} - V_T = \sqrt{2I_D \mu C_{ox} \frac{W}{L}}) \quad (3.6)$$

and body-effect transconductance is described by Equation 3.7.

$$g_{mb} = \frac{\gamma}{2\sqrt{2\phi_f + V_{SB}}}g_m = \chi g_m \quad (3.7)$$

must both be acknowledged for this device [34]. In order to determine the change in threshold voltage for *in vivo* measurements, the measurable impedance change across the piezo is correlated to a change in I_{ds} current across the nMOS. The current drawn from the drain to the source (and vice versa for an alternating current) in the nMOS is then translated to an impedance change in piezoelectric transducer. Therefore, understanding the transconductance seen across the nMOS, and how this varies with exposure to radiation, is of great importance for practical device applications. There is a linear relationship between the top gate transconductance, g_m and threshold voltage, V_t .

Normally, the bulk of a transistor is connected to a ground source, or some constant power supply voltage in MOSFET applications. However, due to the oscillating ultrasonic wave powering of this device, there is a second transconductance formed at the body of the device. This second transconductance is essentially a second gate voltage on the opposite side of the bulk, and will add and subtract to the total transconductance seen across the FET. This body transconductance is also linearly proportional to the threshold voltage. The ratio of g_{mb}/g_m is described in Equation 3.8.

$$\frac{g_{mb}}{g_m} = \chi \quad (3.8)$$

In most cases, χ is in the range of 0.1 to 0.3, meaning that the main transconductance of the FET is seen at the top-gate [34]. In our device, the voltage seen at the bulk will be half of what is seen at the top-gate at any point in the periodic oscillation of the piezo, due to a resistor bridge which halves the input voltage. This resistor bridge is used as a virtual ground for *in vivo* measurements, as demonstrated in [3], [4]. The body-effect transconductance is not investigated within this body of work, but it is important to mention for any implantable dosimeter device in the future when designing a MOSFET dosimeter with an AC voltage seen at the bulk.

The main effect that ionizing radiation has in the MOSFET occurs in the oxide and at the

oxide-silicon interface, however there can be radiation effects in the bulk of the device if there are impurities in the silicon wafer before fabrication. Since silicon wafers are formed with extremely high purity and nearly mono-crystalline structure, it is likely that the body transconductance effects may be ignored when we look at the overall change in transconductance induced by radiation. Further investigation into the oscillating nature of the bulk, and the effect that this has on the radiation induced threshold voltage shifts will need to be done before any implantable version of this device is made.

The radiation damage to the MOSFET is fairly permanent, however, there is some hole annealing at the Si-SiO₂ junction that takes place over time. This annealing can take place over the range of days to months once the device is outside of the radiation environment [28]. Hole annealing will not completely reset the device to the starting device parameters measured before irradiation, but there can be shifts in the ΔV_t and I_{ds} if post-irradiation measurements occur weeks after patient treatment. Thus, it is encouraged to do any post irradiation dosimetry measurements soon after the dose has been received by the Dosimetry Dust device.

Chapter 4

Experimental Verification

4.1 Introduction

The experimental work presented here is a precursor to the implantable dosimeter described in Chapters 2 and 3. The first devices tested at the proton beam were an off-the-shelf nMOS device, ALD1106, connected to a $750 \times 750 \times 750 \mu\text{m}^3$ PZT piezoelectric transducer. The total testing process, from irradiation to ultrasound response, will be described for the ALD1106 devices. Work with the ASIC developed and described by [3], [4] has been started, but radiation shifts and amplitude backscatter results are inconclusive thus far. ASIC work will be further discussed in Chapter 5, Future Directions.

4.2 Off the Shelf nMOS

4.2.1 Experimental Procedure

An off the shelf MOSFET was first chosen for experimentation due to the affordability, availability, and consistency in device performance. By first testing devices with very specific datasheet parameters, it should make testing with the TSMC manufactured Neural Dust devices more streamlined for future work. The nMOS ALD1106 device was chosen due to it's similarity to the Neural Dust motes in terms of threshold voltage ($\approx 0.4V$).

Because of the importance of threshold voltage and I_{ds} shifts in the MOSFET device, it was necessary to design an experimental setup to take IV curves while in a high radiation envi-

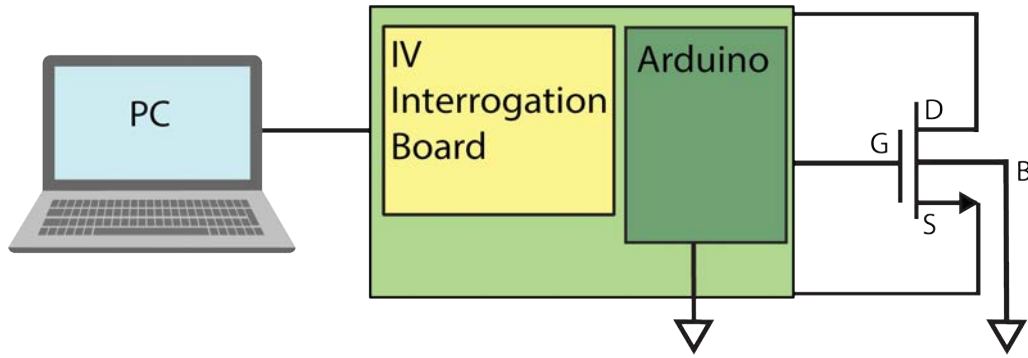


Figure 4.1: For the circuit setup testing for radiation dose response, we are not tying the MOSFET's bulk to an AC source. This is necessary to do initial characterization of the dose response of the MOSFET. The PC was connected to the Arduino and IV interrogation board through the use of a 20 foot USB extension cord to keep it outside of the proton beam therapy room.

ronment. An IV interrogation board (Figure 4.2) was created to work with an Arduino Uno and a MATLAB interface to take these IV curves. A cartoon of the radiation environment setup is shown in Figure 4.1.

Due to the high dose environment, any stray high fluxes of radiation in the dose room can affect current in any integrated circuits, microprocessors, and computers involved in digital data collection. Even the CCD/CMOS cameras used for patient monitoring during irradiation were seen to have the characteristic white dots due to radiation imaging, and are replaced frequently [13], [14]. Therefore, it was best to do all initial testing with an inexpensive, easily replaceable, Arduino setup along with an adjoining breadboarded circuit. All equipment left in the radiation room was shielded as best as possible, and the PC running MATLAB code for data collection was connected to the Arduino by a 20 foot USB extension cord that traversed the outside corridor of the radiation room. The Arduino and IV characterization board (Figure 4.2) was tested between irradiation, due to fluxes that could have damaged any IC components.

The Arduino Uno can provide a maximum of +5V, so the off-the-shelf MOSFET was chosen to work within these parameters. This allowed for a cheap, easy to manufacture data collection setup, but should be discouraged for any fine measurements taken at further development stages where finer measurements are required. The Arduino's step size in this

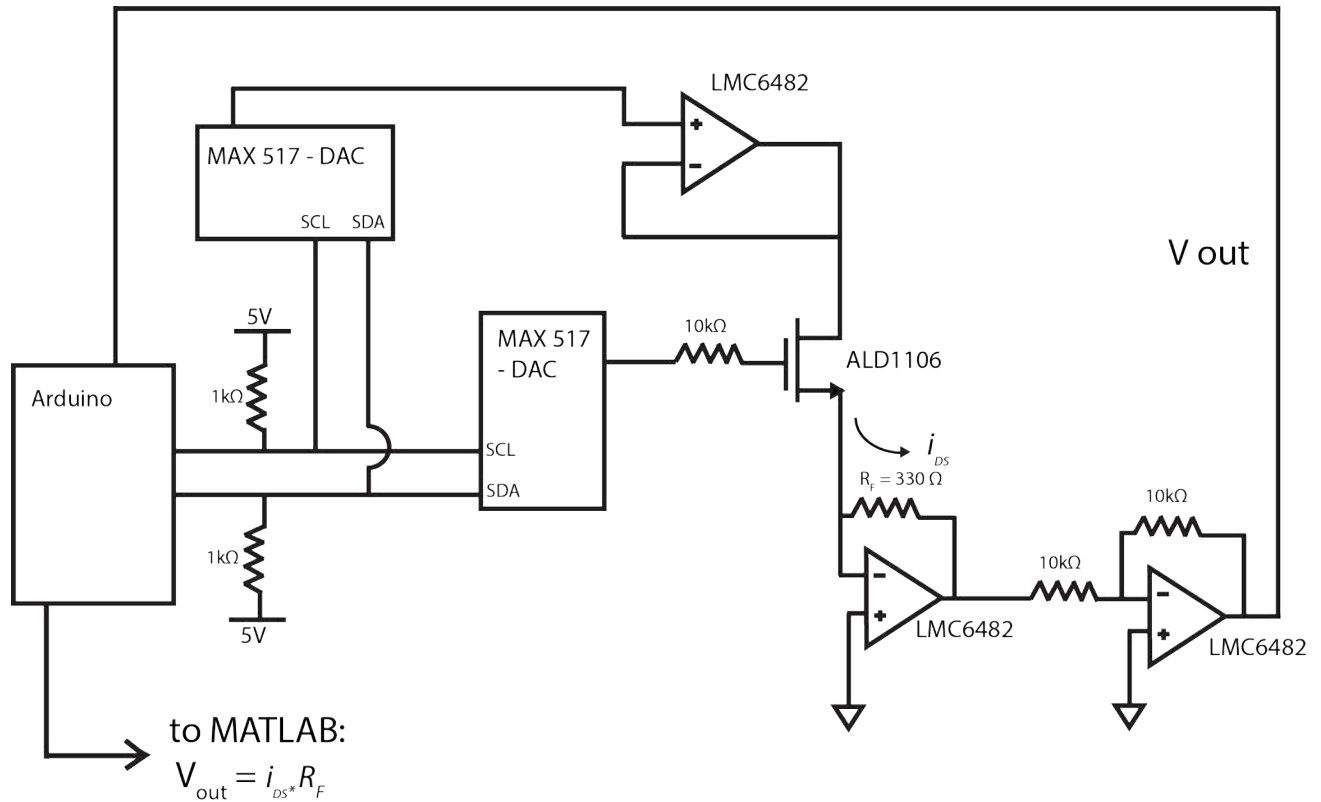


Figure 4.2: IV Interrogation Board for UC Davis. The MAX517 DACs provide the digital to analog conversion from the Arduino. The remainder of the circuit allows for current to be translated to a voltage which can be read in by the Arduino. A MATLAB program was written to read in and plot the IV curves for the MOSFET. $\pm 9V$ rails were provided to the LMC6482 opamps from a set of two 9V batteries, with polarity of one battery switched via the Arduino GND port.

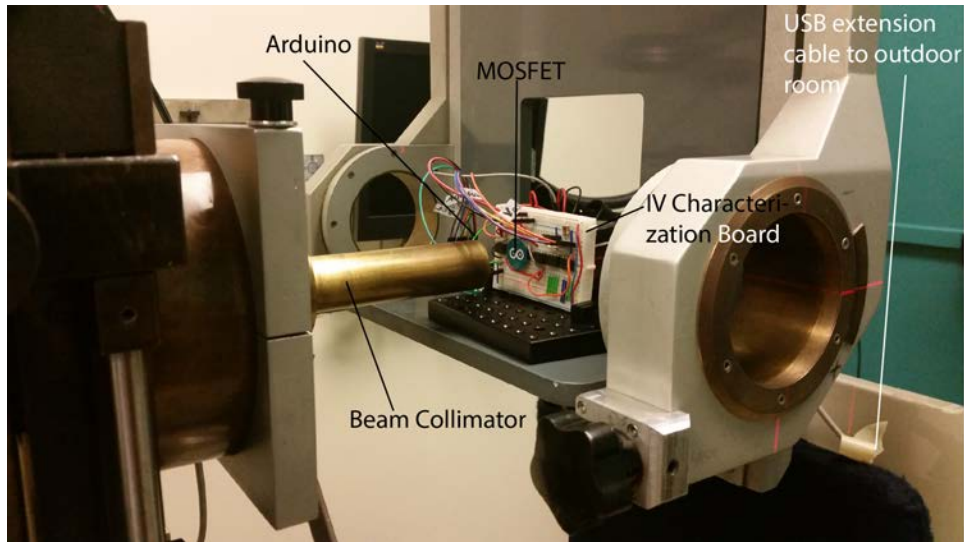


Figure 4.3: Data collection setup at the end of the proton beam. The ALD1106 MOSFET is in its off-the-shelf packaging on the breadboarded circuit and connected to the Arduino. The data collection device is sitting on a shelf that was placed where the patient’s eye would normally be while irradiation takes place. The beam is positioned with a laser cross hair to fall directly on the MOSFET. A long, USB extension cord leads out of the irradiation chamber to the next door room in order to run the MATLAB code during irradiation.

data collection is fairly large, at $5V/255 = 19.6$ mV.

4.2.2 Threshold voltage shift

First, the shift in threshold voltage for the ALD1106 MOSFET is measured. This data was taken at the Crocker Nuclear Facility at UC Davis, with the setup shown in Figure 4.1 and circuit shown in Figure 4.2.

For a standard ocular melanoma treatment, a patient undergoes a total of 4 treatments of 14 Gy each, resulting in 56 Gy total cumulative dose. A patient’s radiation treatment therapy was used below to determine the dose response for the nMOS ALD1106. Devices were irradiated at 14 Gy, 28 Gy, 42 Gy, 56 Gy, and 112 Gy, double the maximum patient treatment. 112 Gy was also examined in order to see if the device would be destroyed at this point. The beam parameters for each of these treatments is shown in Appendix A. IV

data was taken in order to determine the threshold voltage shifts for a set $I_{ds} = 1, 2, 3, 4, 5$ Volts. Figure 4.4 is the raw V_{gs} vs. I_{ds} data taken with the Arduino setup, while Figure 4.5 is a zoomed in version of the raw data in Figure 4.4.

In general, the threshold voltage shifts left for increasing radiation dose. The I_{ds} vs. V_{ds} IV curves in Figure 4.6 were taken concurrently with the data collection of the threshold voltage shifts. The I_{ds} vs. V_{ds} curves show the I_{ds} shifts more clearly than the threshold voltage data.

4.2.3 IV Curves

Because of a negative shift in the nMOS MOSFET's threshold voltage, the amount of current flowing between the drain and the source should increase with an increasing amount of radiation.

As we can see in Figure 4.6, the I_{ds} current quantifiably increases due to MOSFET irradiation. Initially, the I_{ds} current across the MOSFET decreases by 0.15mA in the $V_{gs} = 5V$ curve after the 14 Gy dose is received. The I_{ds} then increases for the remaining doses received. Figure 4.6 implies that I_{ds} is largest when the MOSFET is biased at 5V. The maximum current generated in the device due to dose received is plotted in Figure 4.7. The current generated in Figure 4.7 was taken from the $V_{gs} = 5V$ curve. Maximum post-irradiation current was subtracted from the maximum pre-irradiation current to calculate each data point. The change in current seems to trend linearly as dose is increased, and begins to saturate for doses larger than 56 Gy.

4.2.4 Ultrasonic Backscatter Signal

After the irradiation work at UC Davis's Crocker Nuclear Laboratory, the MOSFETs were brought back to the Maharbiz lab at UC Berkeley to look for changes in the ultrasound backscatter. Figure 4.9 shows water tank setup designed for the work done by Seo, et al. in [2]–[4], while Figure 4.8 is the US backscatter setup used in this project.

A $750\mu m \times 750\mu m \times 750\mu m$ PZT crystal was used in the water tank with the MOSFET's drain and source terminals connected to each end of the piezo.

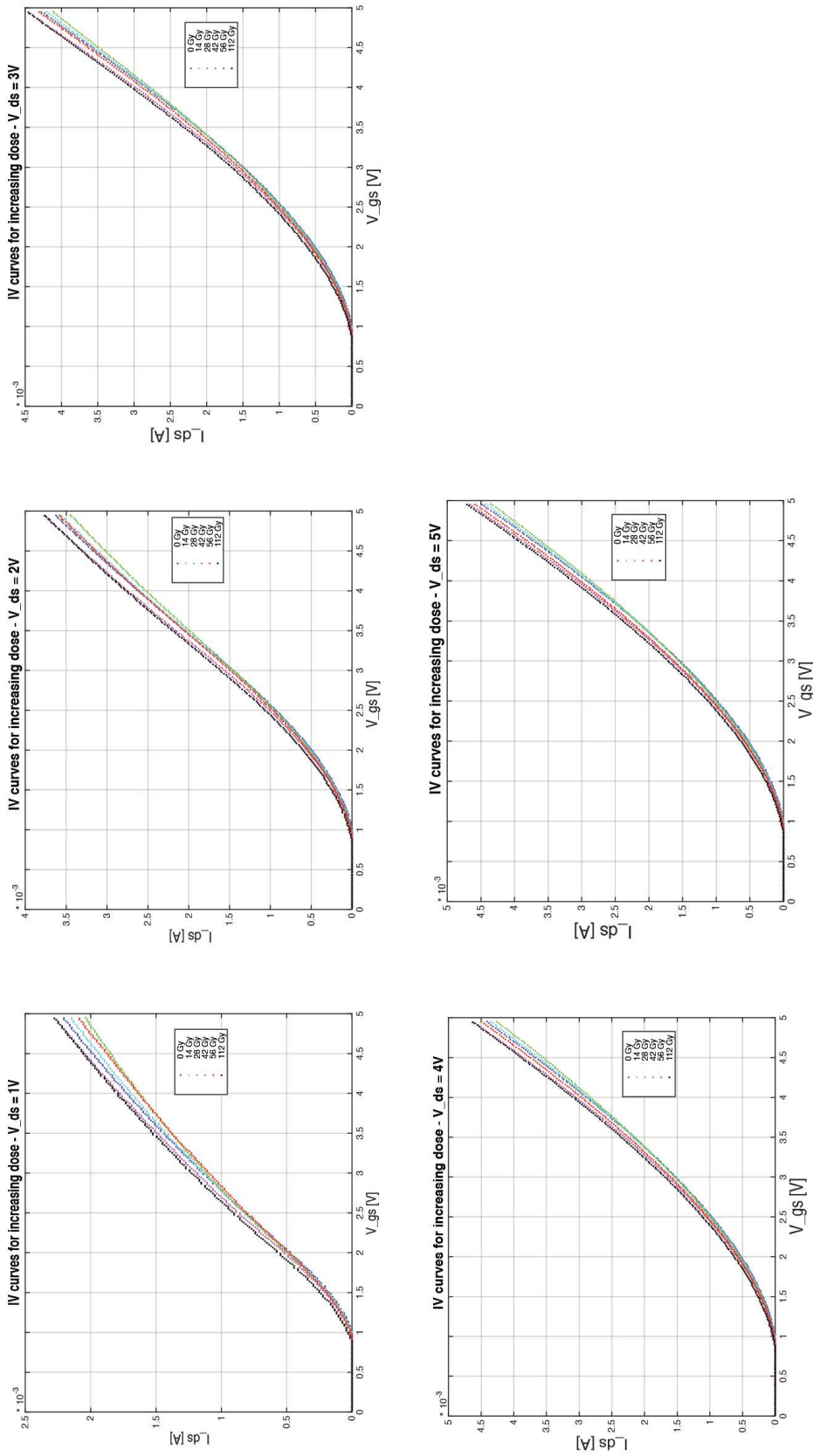


Figure 4.4: Raw data for IV Curves for the ALD1106 when irradiated at the Crocker Nuclear Laboratory's Treatment Plan. There are 4 treatments of 14 Gy each, with a total irradiation dose of 56 Gy. Setting V_{ds} at 1V, 2V, 3V, 4V, and 5V, and plotting IV curves taken after the specified dose was received.

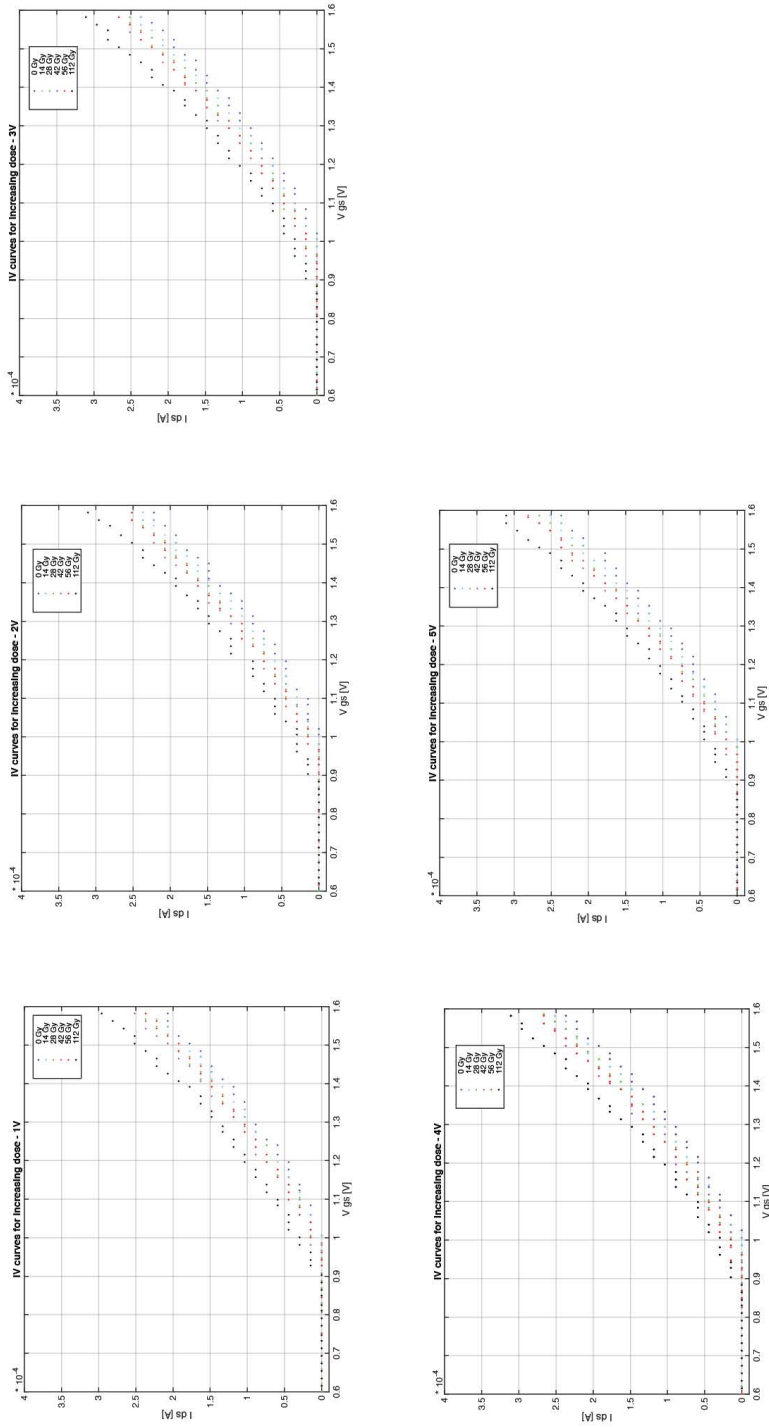


Figure 4.5: Zoomed in version of Figure 4.6. Raw data for IV Curves for the ALD1106 when irradiated at the Crocker Nuclear Laboratory's Treatment Plan. There are 4 treatments of 14 Gy each, with a total irradiation dose of 56 Gy. Setting V_{ds} at 1V, 2V, 3V, 4V, and 5V, and plotting IV curves taken after the specified dose was received.

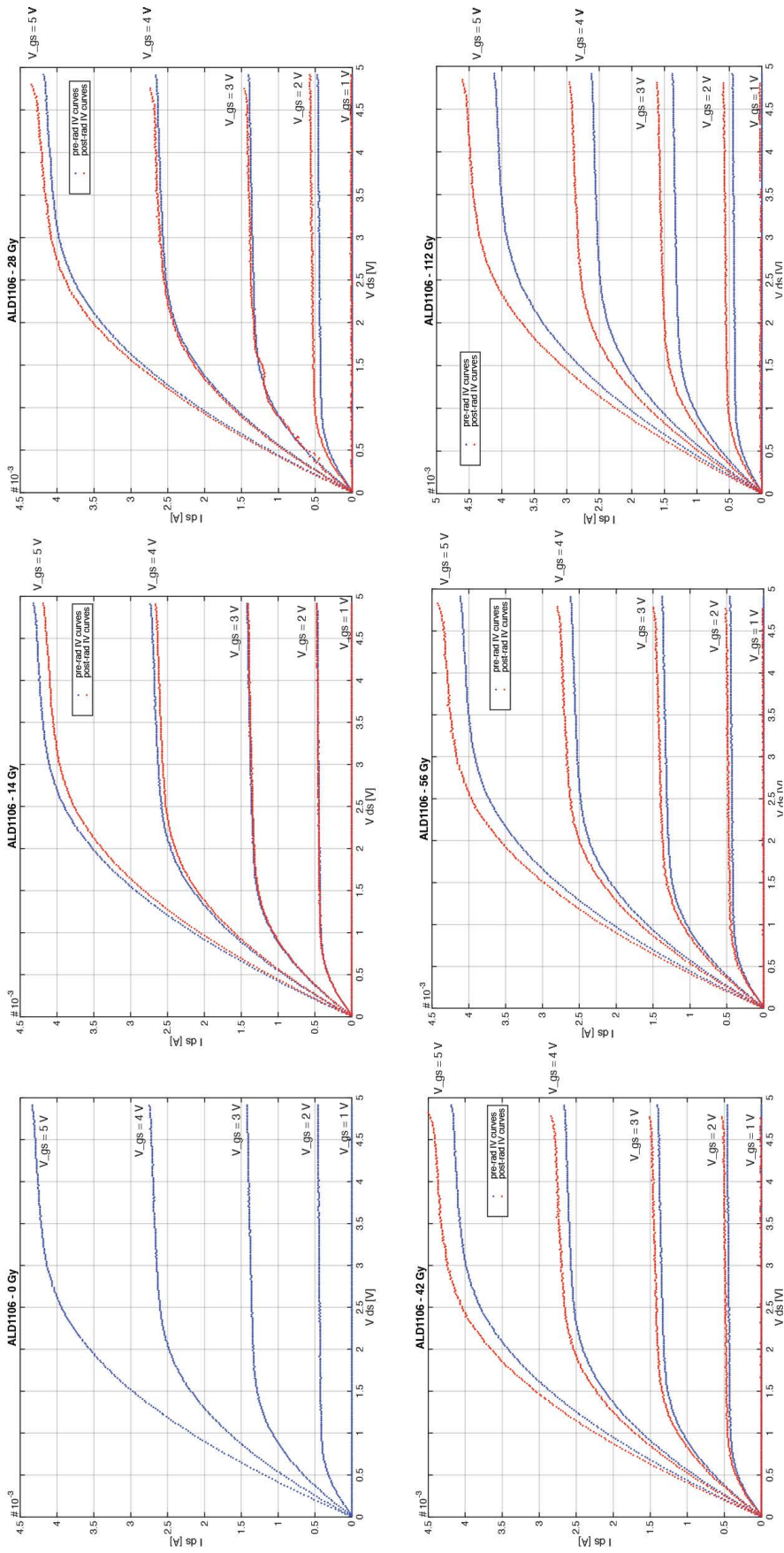


Figure 4.6: IV Curves for the ALD1106 when irradiated at the Crocker Nuclear Laboratory's Treatment Plan. There are 4 treatments of 14 Gy each, with a total irradiation dose of 56 Gy. Varying V_{gs} , and plotting I_{ds} current vs. V_{ds} .

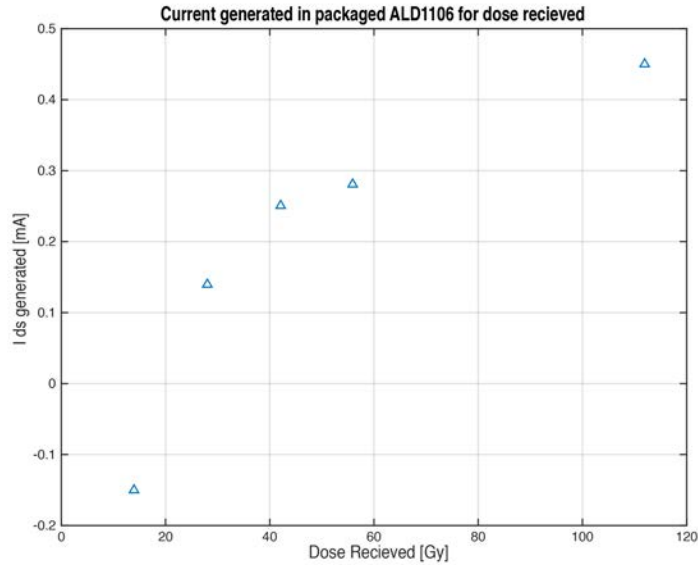


Figure 4.7: ΔI_{ds} current generated in the packaged ALD1106 off-the-shelf device as a function of the dose recieved. This is the maximum current shift due to irradiation, seen when the MOSFET is fully biased at $V_{gs} = 5V$.

The piezo is prepared for the water tank by wirebonding each end of the piezo to a PCB pinout, and encapsulating the piezo with a UV hardening epoxy.

The steps taken for US water tank testing are described below.

1. A piezoelectric transducer is placed within the water tank for alignment (Figure 4.10A)
2. The ASIC designed by Seo and used in [4] is supplied 67mA to the +5V terminal, 41mA to the -5V terminal, and 41mA to the +3.3V terminal. (Figure 4.10B)
3. The function generator supplies a square wave clock function at 7.2MHz. The ASIC has a setting which both halves and quarters this incoming frequency for the ultrasound transducer. The outgoing US transducer wave from the ASIC is 1.85MHz. (Figure 4.10C)
4. A $\pm 20V$ is sent to amplify the outgoing function generator waveform that will communicate with the piezo in the water tank.

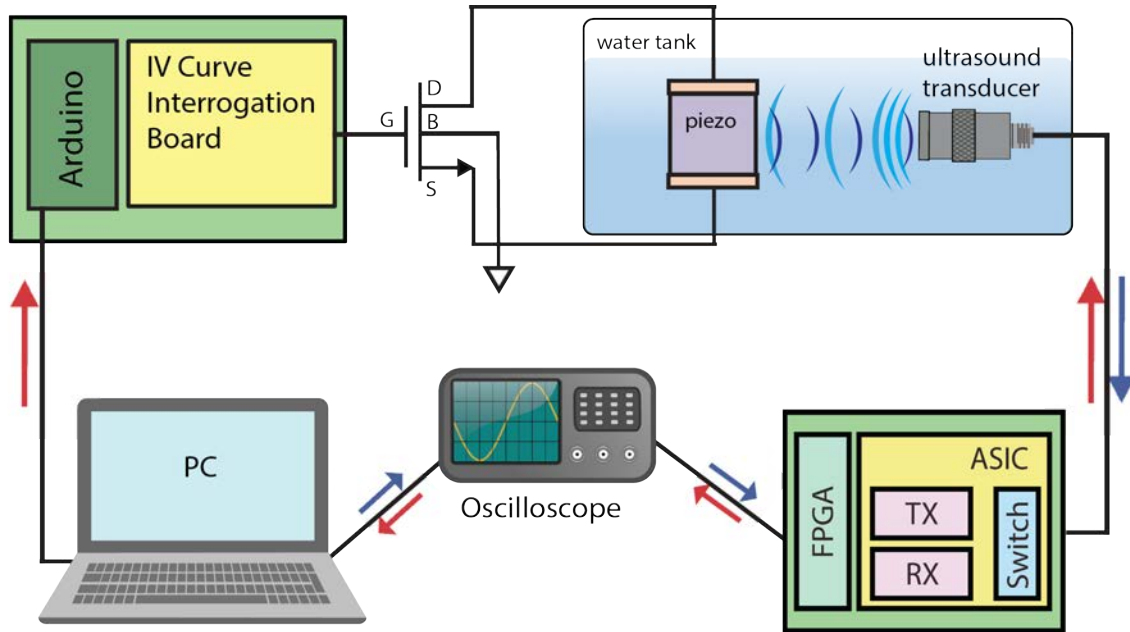


Figure 4.8: Ultrasound Testing setup used to obtain the backscatter data for before and after irradiation. The FPGA interrogation board was designed and tested by Seo, et. al. in [3], [4]. The irradiated MOSFET is left outside of the water tank in this setup (due to being an off the shelf device ill suited for water testing), and connected to a piezo within the water tank to characterize the backscatter response.

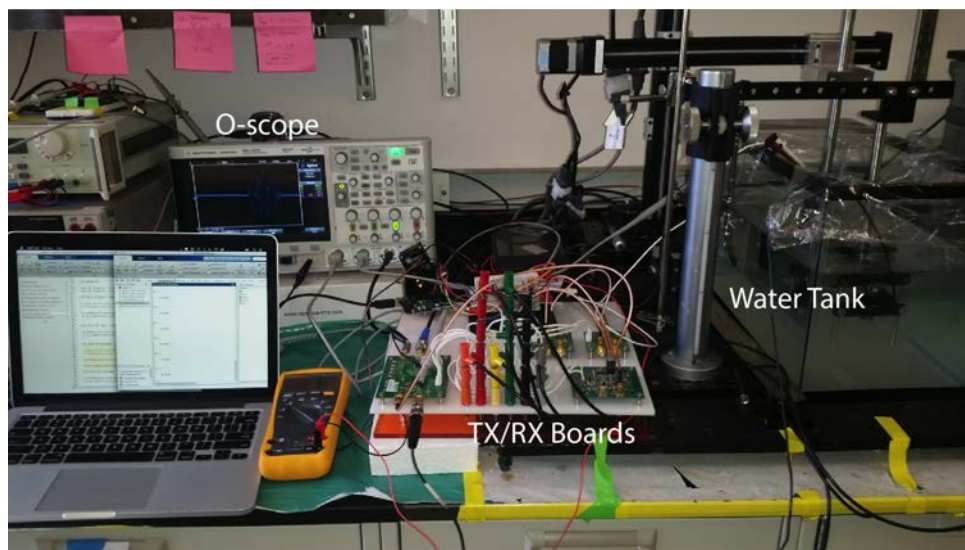


Figure 4.9: Maharbiz Lab water tank setup designed for the work done by Seo, et al. in [1,2,3].

5. IMPORTANT: When the FPGA is enabled, the high $\pm 20V$ will go to the ultrasound transducer (model: V323-SU, Olympus). The transducer **must** be in the water before the FPGA is enabled. If not, very large, high voltage reflections will occur within the transducer and damage the US transducer's crystal.
6. The x,y, and z axes are moved on the piezo to align it with the US pulse from the transducer. Ideally, there should be about $6 \mu s$ between the transducer and the piezo for a 1.85MHz interrogation pulse.
7. Check the power harvested by the piezo by connecting it directly to the oscilloscope. Align the piezo at resonance by finding the maximum amplitude of backscatter in x, y, and z. This is indicated by the green curve in Figure 2.2.B. Once power harvested is maximized, backscatter data may be obtained.
8. Take data from the backscatter amplitude from the piezo from the US transducer. An example is shown in Figure 2.2.C.

The piezo is flanked by a period of no amplitude shift on either side of the piezo, due to encapsulation epoxy on one end, and a PCB board holding the piezo on the other. In order to determine where the piezo is within the entire backscatter signal, one can bias the MOSFET within the device and visually determine where the amplitude shifts downward. US backscatter due to the epoxy and the PCB will not show any change in amplitude when the MOSFET is biased, which makes the piezo's region of interest easy to find visually. Figure 4.11A shows the raw backscatter data when looking at the oscilloscope. This data is then centered around the backscatter pulse by visual inspection on an oscilloscope, as shown in Figure 4.11B.

Once the backscatter pulse data from the oscilloscope is received by the computer, a MATLAB windowing function performs the data analysis as follows:

1. Absolute value of the raw data is taken
2. MATLAB function "max" is used to find the maximum voltage spike within the backscatter pulse and the time at which this occurs
3. Visual inspection of the raw data determines what the windowing should be around this maximum pulse in order to capture the entire piezo's amplitude response

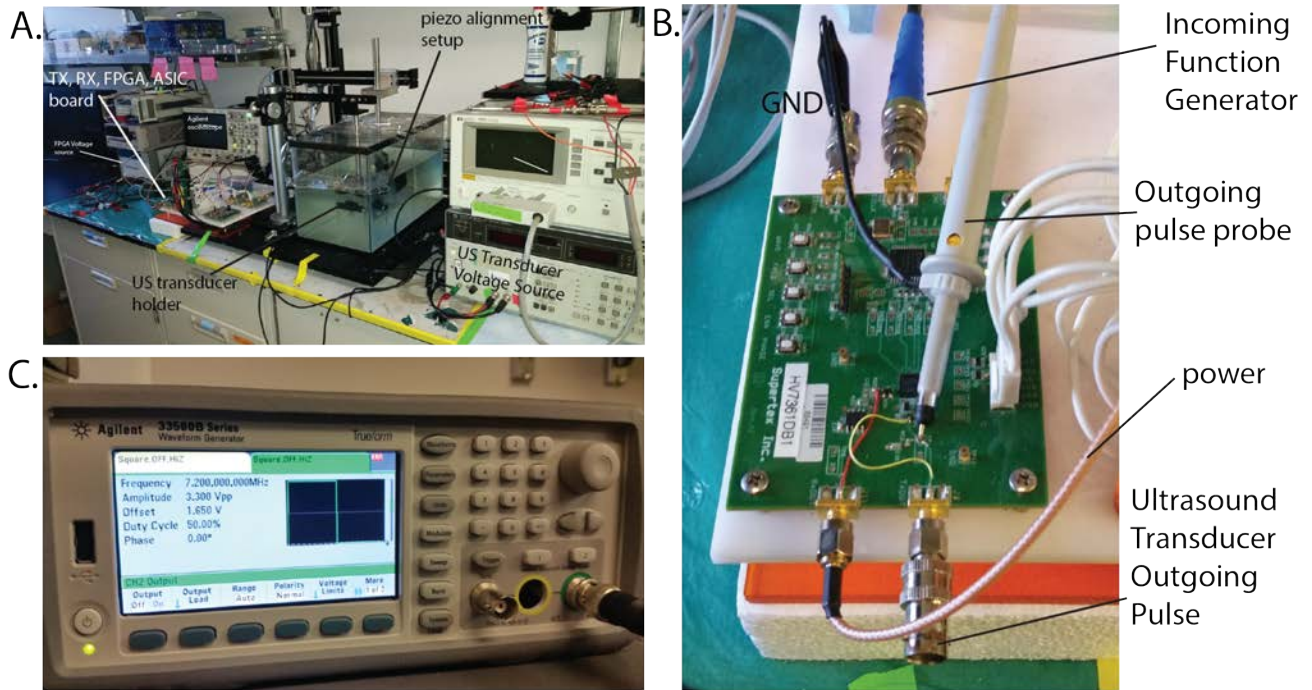


Figure 4.10: A. Overall view of the water tank setup. A piezoelectric transducer, $750\mu\text{m} \times 750\mu\text{m} \times 750\mu\text{m}$ PZT crystal, is placed in the water tank for alignment B. ASIC designed by Seo. The ASIC mainly varies the function generator pulse in frequency and amplitude in order to vary the US transducer output pulse C. Function generator output settings. A 7.8MHz square wave is divided by the ASIC to create a 1.85MHz pulse used for these experiments. The backscatter input pulse is shown in Figure 2.2.A.

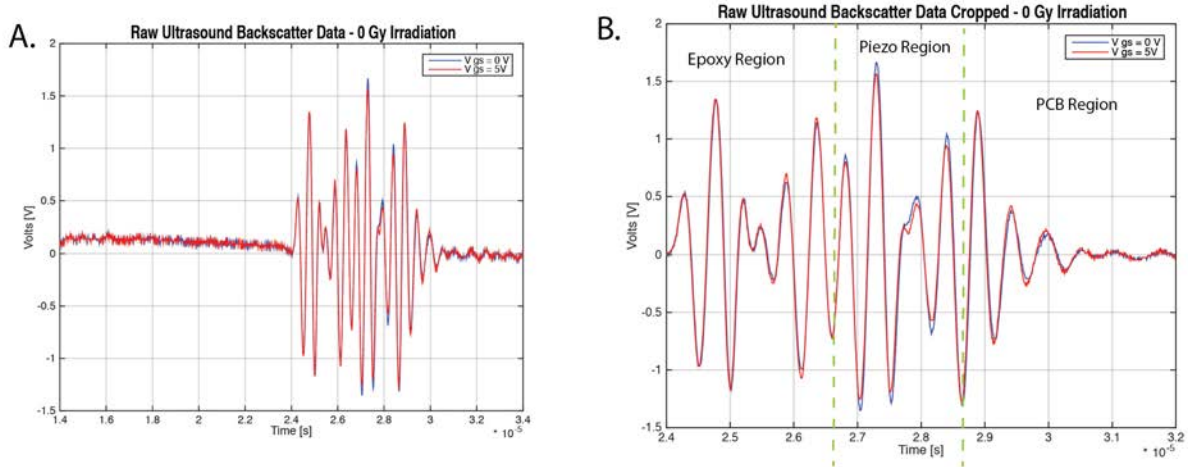


Figure 4.11: A. Scope Raw Data for US Backscatter pulse with a 5V V_{gs} bias (red) and 0V V_{gs} bias (blue). B. Scope centered around backscatter pulse. The region with an amplitude shift between the 5V V_{gs} bias (red) and 0V V_{gs} bias (blue) is the piezo region. To the left of this region are US backscatter due to the epoxy, and to the right is the US backscatter due to the PCB.

- Area under each pulse is determined by numerical integration using the trapezoidal method in Equation 4.1.

$$\int_b^a f(x)dx \approx \frac{b-a}{2N} \sum_{n=1}^N (f(x_n) + f(x_{n+1})) \quad (4.1)$$

Raw data of the piezo after this windowing function is shown in Figure 4.12. Figure 4.6 implies that I_{ds} is largest when the MOSFET is biased at 5V, and will cause the largest amplitude shift in the piezo. The 5V bias was compared to a bias of 0V in order to determine what the amplitude shift is in each irradiation step.

The amount of amplitude shift is calculated by taking a ratio shown in Equation 4.2

$$\text{Area shrinkage} = 100 \times \left(1 - \frac{\text{Trapezoidal Area at 5 V bias}}{\text{Trapezoidal Area when device off (0V bias)}} \right) \quad (4.2)$$

The area shrinkage percentage is plotted in Figure 4.13. Note that as the radiation dose

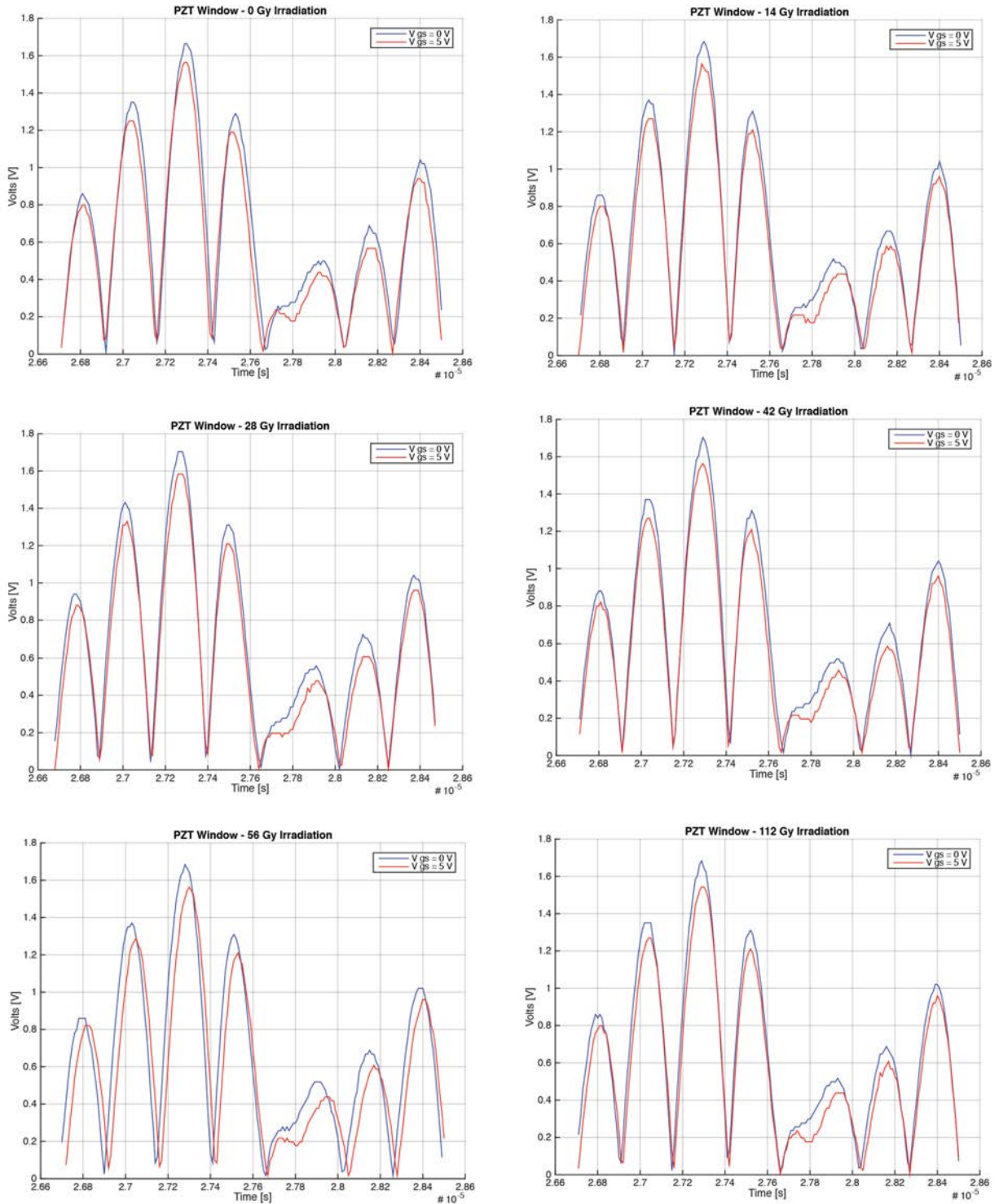


Figure 4.12: Raw Backscatter Data windowed to the piezo. A bias of 5 Volts is compared to a 0 volt bias for each irradiation. The piezo backscatter was determined to within the period $t = [2.67, 2.85] \times 10^{-5}$

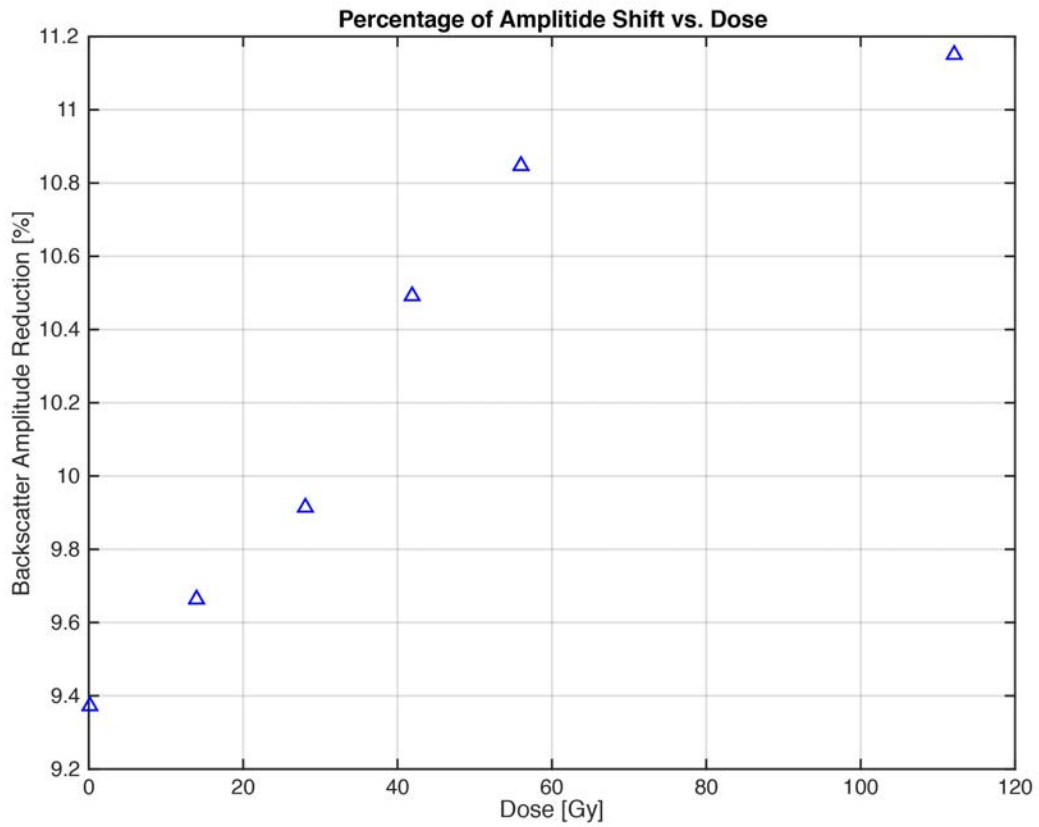


Figure 4.13: Area shrinkage plotted as a function of the dose recieved. This characterization curve corresponds to the amplitude shift of the device when it is on and biased at 5V versus off (biased at 0V).

increases, the amount of shrinkage in the backscatter pulse also increase somewhat linearly, before leveling off around 60Gy. The percentage of decrease in the US backscatter amplitude is subtle with this setup, with the ΔA range of $\approx 1.8\%$ between a dose of 0 Gy and a dose of 112 Gy. With improvements to SNR in the US setup, it is expected that the backscatter amplitude shifts will be more dramatic. Methods of reducing noise mainly include reducing the parasitic capacitance caused by the electrical leads connecting the MOSFET outside of the water tank to the piezo inside of the water tank. This parasitic will not be within the actual implantable devices, which has the MOSFET wirebonded with the piezo on a single board.

In the AC implantable version of device, a characterization curve like the one in Figure 4.13 will need to be made for multiple V_{gs} bias voltages on the MOSFET. As long as the device is pinged and read out at a known bias voltage that has a corresponding empirically created Amplitude vs. Dose characterization curve, the *in vivo* dose recieved by the device can be determined.

Chapter 5

Conclusions

A fully implantable, wireless dosimeter is a crucial step towards a closed-loop *in vivo* dosimetry device. This work presents the feasibility of the ultrasound backscatter MOSFET dosimeter idea for implantation, and suggests an easy path forward to create and test the fully implantable device using proton beam ocular melanoma treatments at Crocker Nuclear Laboratory. The off-the-shelf nMOS ALD1106 devices went through the entire engineering strategy presented in Chapter 3. Threshold voltage shifts, I_{ds} current flow, and the US backscatter communication were tested for the various dosages corresponding to the UCSF/UCD ocular melanoma treatment described in [7], [13], [14].

The data collected supports the following general trends:

1. As dose is increased, the threshold voltage V_t decreases and shifts to the left of the starting position
2. As dose is increased, I_{ds} increases somewhat linearly (Figure 4.7).
3. As dose is increased, the backscatter amplitude shifts linearly until approximately 60 Gy, after which the amplitude shift started to taper off (Figure 4.12).

The work presented here is only a precursor to a fully implantable device which incorporates a MOSFET and piezoelectric transducer in the same package. The effect that body effect transconductance has on irradiated device performance will need to be investigated for the fully implantable device as well.

The device's sensitivity and dose range is mainly dependant on the SiO₂ oxide growth step during CMOS fabrication, given that radiation induced shifts in V_t and I_{ds} is highly dependant on the creation of interface traps and oxide traps in the Silicon/Silicon Dioxide layer in CMOS devices. This is discussed further in Section 3.1.1. Future experimental work with this oxide growth step can lead to insights on parameters for creating interesting dosimeters at different dose ranges and device sensitivity. Since the MOSFET is the only part of the device that needs to be tailored to radiation specifications, many different dose ranges and dose sensitivities can be attached to the piezo to create dosimeters for a wide variety of radiation oncology applications.

Lastly, it would be worth developing multiple characterization curves (dose vs. amplitude backscatter shift) for the 0V to $\pm 0.8V$ bias voltage that will be seen on the gate while ping-ing the MOSFET *in vivo*. With the amplitude backscatter determined for a specific dose at a specific bias voltage, one can infer the dose recieved at the site of the implanted device.

Although there is a long way to go in terms of developing a fully implantable device specific to the 56 Gy dose range needed by UCSF/UCD proton beam therapy ocular melanoma treatments, the work presented here may be a good starting point in future implantable dosimetry endeavors.

5.1 Future Work - Dosimetry Dust Mote

Work on the fully implantable devices has been started as of 2017. Figure 2.1 in the section on Ultrasonic Power Transfer is a sample device that was prepared with a piezo attached. Most of the work involving sample preparation has utilized a breakout board, as shown in Figure 5.1.

It is suggested that initial radiation testing is done on these breakout boards without the piezo in order to control the variation in backscatter that can be caused by physical variations in the piezo and piezo misalignments. Testing in Chapter 4 was performed with the same piezo in the water tank to initially control for these issues.

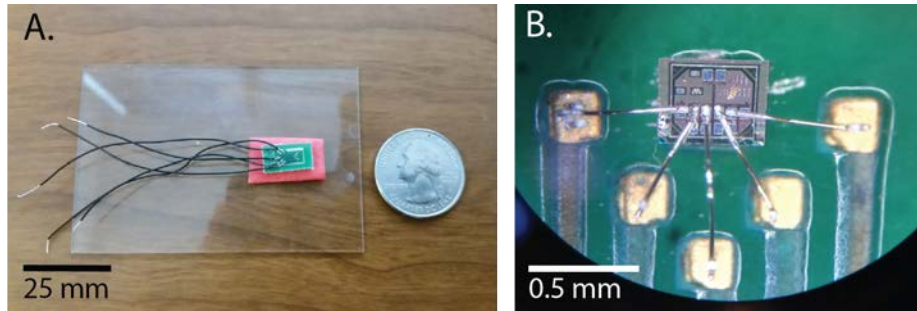


Figure 5.1: A. Breakout board designed for the piezo for IV characterization of the ASIC. B. Zoom of the wirebonded nMOS device (This die is a reflected version of the die in Figure 2.1. During assembly, take note of the die orientation and flip of wirebonding pads Bulk, Source, Center, Drain, and Gate.

The nMOS devices in Figure 5.1 were brought to Crocker Nuclear Laboratory for the same irradiation treatment done on the ALD1106 devices, however, the post-radiation results were inconclusive for the first round of testing. Many of the devices ceased to perform post-radiation, which is likely due to radiation induced latchup effects as well as far too much radiation damage at the Si-SiO₂ interface within the initial 14Gy treatment. For future work in this area it is suggested to start with irradiating the devices in the range of 0-1Gy prior to moving towards larger doses. It is also suggested to investigate the dose response of the nMOS ASIC device with other types of radiation from readily available isotopes. For example, one may try a strontium-90 β emitters, a cobalt-60 γ emitter, or even a mixed emitter such as caesium-137 which decays by both β and γ . All three of these radioisotopes are commonly found in small micro-curie amounts, as they are typically used for calibration of radiation detectors.

References

- [1] I. K. Daftari, K. K. Mishra, J. M. O'Brien, T. Tsai, S. S. Park, M. Sheen, and T. L. Phillips, "Fundus image fusion in eyeplan software: an evaluation of a novel technique for ocular melanoma radiation treatment planning," *Medical physics*, vol. 37, no. 10, pp. 5199–5207, 2010.
- [2] D. Seo, J. M. Carmena, J. M. Rabaey, E. Alon, and M. M. Maharbiz, "Neural Dust: An Ultrasonic, Low Power Solution for Chronic Brain-Machine Interfaces," *ArXiv e-prints*, Jul. 2013. arXiv: 1307.2196 [q-bio.NC].
- [3] D. Seo, J. M. Carmena, J. M. Rabaey, M. M. Maharbiz, and E. Alon, "Model validation of untethered, ultrasonic neural dust motes for cortical recording," *Journal of neuroscience methods*, vol. 244, pp. 114–122, 2015.
- [4] D. Seo, R. M. Neely, K. Shen, U. Singhal, E. Alon, J. M. Rabaey, J. M. Carmena, and M. M. Maharbiz, "Wireless recording in the peripheral nervous system with ultrasonic neural dust," *Neuron*, vol. 91, no. 3, pp. 529–539, 2016.
- [5] K. Shen, "Assembly of a Wireless Ultrasonic Backscatter System," Master's thesis, UC Berkeley, Berkeley, California, 2016.
- [6] I. Daftari, T. Renner, L. Verhey, R. Singh, M Nyman, P. Petti, and J. Castro, "New ucsf proton ocular beam facility at the crocker nuclear laboratory cyclotron (uc davis)," *Nuclear Instruments and Methods in Physics Research Section A: Accelerators, Spectrometers, Detectors and Associated Equipment*, vol. 380, no. 3, pp. 597–612, 1996.
- [7] K. K. Mishra, I. K. Daftari, V. Weinberg, T. Cole, J. M. Quivey, J. R. Castro, T. L. Phillips, and D. H. Char, "Risk factors for neovascular glaucoma after proton beam therapy of uveal melanoma: a detailed analysis of tumor and dose–volume parameters," *International Journal of Radiation Oncology* Biology* Physics*, vol. 87, no. 2, pp. 330–336, 2013.

- [8] National Institute of Standards and Technology, *Physical Measurements Laboratory. PSTAR - Stopping power and range tables for protons*. <https://physics.nist.gov/PhysRefData/Star/Text/PSTAR.html>, Accessed: 2017-12-08.
- [9] M. F. L'Annunziata, *Radioactivity: introduction and history*. Elsevier, 2007.
- [10] D. Jette and W. Chen, "Creating a spread-out bragg peak in proton beams," *Physics in medicine and biology*, vol. 56, no. 11, N131, 2011.
- [11] K. Yamoah and P. A. Johnstone, "Proton beam therapy: clinical utility and current status in prostate cancer," *OncoTargets and therapy*, vol. 9, p. 5721, 2016.
- [12] D. Davino, "Theory, design and tests on a prototype module of a compact linear accelerator for hadrontherapy," 2002.
- [13] "Lbnl systems for charged particle radiotherapy/radiobiology since the closing of the bevalac," UC San Francisco, UC Davis, Tech. Rep., 2003.
- [14] I. K. Daftari, K. K. Mishra, R. P. Singh, D. J. Shadoan, and T. L. Phillips, "An overview of the control system for dose delivery at the ucsf dedicated ocular proton beam," *International Journal of Medical Physics, Clinical Engineering and Radiation Oncology*, vol. 5, no. 04, p. 242, 2016.
- [15] E. Villani, M Crepaldi, D. Demarchi, A Gabrielli, A Khan, E Pikhay, Y Roizin, A Rosenfeld, and Z. Zhang, "A monolithic 180 nm cmos dosimeter for wireless in vivo dosimetry," *Radiation Measurements*, vol. 84, pp. 55–64, 2016.
- [16] C. W. Scarantino, D. M. Ruslander, C. J. Rini, G. G. Mann, H. T. Nagle, and R. D. Black, "An implantable radiation dosimeter for use in external beam radiation therapy," *Medical physics*, vol. 31, no. 9, pp. 2658–2671, 2004.
- [17] R Ramaseshan, K. Kohli, T. Zhang, T Lam, B Norlinger, A Hallil, and M Islam, "Performance characteristics of a micromosfet as an in vivo dosimeter in radiation therapy," *Physics in medicine and biology*, vol. 49, no. 17, p. 4031, 2004.
- [18] B. Mijnheer, S. Beddar, J. Izewska, and C. Reft, "In vivo dosimetry in external beam radiotherapy," *Medical physics*, vol. 40, no. 7, 2013.
- [19] A.-C. Knopf and A. Lomax, "In vivo proton range verification: a review," *Physics in medicine and biology*, vol. 58, no. 15, R131, 2013.

- [20] G. P. Beyer, G. G. Mann, J. A. Pursley, E. T. Espenhahn, C. Fraisse, D. J. Godfrey, M. Oldham, T. B. Carrea, N. Bolick, and C. W. Scarantino, "An implantable mosfet dosimeter for the measurement of radiation dose in tissue during cancer therapy," *IEEE Sensors Journal*, vol. 8, no. 1, pp. 38–51, 2008.
- [21] *Best Medical Canada Products - MobileMOSFET On-line Wireless Dosimetry*. http://www.bestmedicalcanada.com/product_mobilemos.html, Accessed: 2017-12-08.
- [22] *Best Medical Canada Products - Portable Dosimeter Model TN-RD-90*, http://www.bestmedicalcanada.com/product_portable.html, Accessed: 2017-12-08.
- [23] A. Denisov and E. Yeatman, "Ultrasonic vs. inductive power delivery for miniature biomedical implants," in *Body Sensor Networks (BSN), 2010 International Conference on*, IEEE, 2010, pp. 84–89.
- [24] B. Warneke, M. Last, B. Liebowitz, and K. S. Pister, "Smart dust: communicating with a cubic-millimeter computer," *Computer*, vol. 34, no. 1, pp. 44–51, 2001.
- [25] B. A. Warneke, M. D. Scott, B. S. Leibowitz, L. Zhou, C. L. Bellew, J. A. Chediak, J. M. Kahn, B. E. Boser, and K. S. Pister, "An autonomous 16 mm/sup 3/solar-powered node for distributed wireless sensor networks," in *Sensors, 2002. Proceedings of IEEE*, IEEE, vol. 2, 2002, pp. 1510–1515.
- [26] J. M. Kahn, R. H. Katz, and K. S. Pister, "Emerging challenges: mobile networking for smart dust," *Journal of Communications and Networks*, vol. 2, no. 3, pp. 188–196, 2000.
- [27] G. D. Ludwig, "The velocity of sound through tissues and the acoustic impedance of tissues," *The Journal of the Acoustical Society of America*, vol. 22, no. 6, pp. 862–866, 1950.
- [28] T.-P. Ma and P. V. Dressendorfer, *Ionizing radiation effects in MOS devices and circuits*. John Wiley & Sons, 1989.
- [29] J. R. Srour and J. M. McGarrity, "Radiation effects on microelectronics in space," *Proceedings of the IEEE*, vol. 76, no. 11, pp. 1443–1469, 1988.
- [30] A B. Rosenfeld, "Mosfet dosimetry on modern radiation oncology modalities," *Radiation protection dosimetry*, vol. 101, no. 1-4, pp. 393–398, 2002.

- [31] R. Consorti, A. Petrucci, F. Fortunato, A. Soriani, S. Marzi, G. Iaccarino, V. Landoni, and M. Benassi, “In vivo dosimetry with mosfets: dosimetric characterization and first clinical results in intraoperative radiotherapy,” *International Journal of Radiation Oncology* Biology* Physics*, vol. 63, no. 3, pp. 952–960, 2005.
- [32] M Soubra, J Cygler, and G Mackay, “Evaluation of a dual bias dual metal oxide-silicon semiconductor field effect transistor detector as radiation dosimeter,” *Medical physics*, vol. 21, no. 4, pp. 567–572, 1994.
- [33] M. S. Andjelković, G. S. Ristić, and A. B. Jakšić, “Using radfet for the real-time measurement of gamma radiation dose rate,” *Measurement Science and Technology*, vol. 26, no. 2, p. 025 004, 2015.
- [34] P. R. Gray, P. Hurst, R. G. Meyer, and S. Lewis, *Analysis and design of analog integrated circuits*. Wiley, 2001.

Appendices

Appendix A

Proton Beam Parameters

FET2

PATIENT TREATMENT SUMMARY SHEET

LF: [225,251]E169997S1.011

PATIENT NAME: STEFANIE EXPT
PATIENT I.D.: E169997S1.011

DATE: 10-JUN-16
TIME: 12:30:31

SPREAD BRAGG PEAK WIDTH 2.00 CM.

AVAILABLE RANGE OF BEAM 3.00 CM.

REQUESTED RESIDUAL RANGE 1.99 CM.

WATER COLUMN SETTING 1.01 CM.

TREATMENT TIME 2.22 MIN.

DOSE (cGy) PRESCRIBED AT ISO-CENTER....	1273.0	
IC2 DOSE (cGy) AT ISO-CENTER	1274.8	100.1 %
IC1 DOSE (cGy) AT ISO-CENTER	1279.4	100.5 %
DOSE (cGy) VARIANCE AT ISO-CENTER (+/-)	1.7	

OPERATOR COMMENTS: 7NA BEAM CURRENT

DONE BY: IKD

14G/E

NEW ICFs	(C O U N T S / R A D)		
	10-JAN-16	AT	05:22:23
WC	SEM	IC1SUM	IC2SUM
0.00	12.789	603.356	403.295

OLD ICFs	(C O U N T S / R A D)		
	10-JUN-16	AT	12:22:23
WC	SEM	IC1SUM	IC2SUM
0.00	12.789	603.356	403.295

NEW/OLD AVG. 1.000 1.000 1.000

PCFs	(C O U N T S / R A D)		
	10-JUN-16	AT	12:22:23
WC	SEM	IC1SUM	IC2SUM
1.01	23.379	1119.365	954.334

WATER COLUMN VALUE		SEM COUNTS	IC1SUM COUNTS	IC2SUM COUNTS
1.01	EXP	29761.404	1424951.625	1214866.750
1.01	REC	29857.295	1432110.000	1216582.250

FET3

PATIENT TREATMENT SUMMARY SHEET

LF: [225,251]E169997S1.011

PATIENT NAME: STEFANIE EXPT
PATIENT I.D.: E169997S1.011

DATE: 10-JUN-16
TIME: 12:41:14

SPREAD BRAGG PEAK WIDTH 2.00 CM.
AVAILABLE RANGE OF BEAM 3.00 CM.
REQUESTED RESIDUAL RANGE 1.99 CM.
WATER COLUMN SETTING 1.01 CM.
TREATMENT TIME 2.24 MIN.

DOSE (cGy) PRESCRIBED AT ISO-CENTER.... 2546.0
IC2 DOSE (cGy) AT ISO-CENTER 2549.9 100.2 %
IC1 DOSE (cGy) AT ISO-CENTER 2570.0 100.9 %
DOSE (cGy) VARIANCE AT ISO-CENTER (+/-) 12.9

OPERATOR COMMENTS: exPT 2 14 NA BEAM CURRENT

DONE BY: IKD

42 GYE
286 GYE

NEW ICFs (C O U N T S / R A D)
10-JAN-16 AT 05:22:23
WC SEM IC1SUM IC2SUM
0.00 12.789 603.356 403.295

OLD ICFs (C O U N T S / R A D)
10-JUN-16 AT 12:22:23
WC SEM IC1SUM IC2SUM
0.00 12.789 603.356 403.295

NEW/OLD AVG. 1.000 1.000 1.000

PCFs (C O U N T S / R A D)
10-JUN-16 AT 12:22:23
WC SEM IC1SUM IC2SUM
1.01 23.379 1119.365 954.334

WATER COLUMN VALUE
1.01 EXP 59522.809 2849903.250 2429733.500
1.01 REC 60390.285 2876737.250 2433458.250

FET4

PATIENT TREATMENT SUMMARY SHEET

LF: [225,251]E169997S1.011

PATIENT NAME: STEFANIE EXPT
PATIENT I.D.: E169997S1.011

DATE: 10-JUN-16
TIME: 12:49:41

SPREAD BRAGG PEAK WIDTH 2.00 CM.
AVAILABLE RANGE OF BEAM 3.00 CM.
REQUESTED RESIDUAL RANGE 1.99 CM.
WATER COLUMN SETTING 1.01 CM.

TREATMENT TIME 3.26 MIN.

DOSE (cGy) PRESCRIBED AT ISO-CENTER.... 3819.0
IC2 DOSE (cGy) AT ISO-CENTER 3822.6 100.1 %
IC1 DOSE (cGy) AT ISO-CENTER 3843.8 100.6 %
DOSE (cGy) VARIANCE AT ISO-CENTER (+/-) 16.0

42 GYE

OPERATOR COMMENTS: BEAM CURRENT 14 NA 42 GYe DOSE

DONE BY: IKD

NEW ICFs (COUNTS / RAD)
10-JAN-16 AT 05:22:23
WC SEM IC1SUM IC2SUM
0.00 12.789 603.356 403.295

OLD ICFs (COUNTS / RAD)
10-JUN-16 AT 12:22:23
WC SEM IC1SUM IC2SUM
0.00 12.789 603.356 403.295

NEW/OLD AVG. 1.000 1.000 1.000

PCFs (COUNTS / RAD)
10-JUN-16 AT 12:22:23
WC SEM IC1SUM IC2SUM
1.01 23.379 1119.365 954.334

WATER COLUMN VALUE SEM COUNTS IC1SUM COUNTS IC2SUM COUNTS
1.01 EXP 89284.211 4274855.000 3644600.000
1.01 REC 88362.547 4302613.000 3647992.750

FETS

PATIENT TREATMENT SUMMARY SHEET

LF: [225,251]E169997S1.011

PATIENT NAME: STEFANIE EXPT
PATIENT I.D.: E169997S1.011

DATE: 10-JUN-16
TIME: 12:59:37

SPREAD BRAGG PEAK WIDTH 2.00 CM.

AVAILABLE RANGE OF BEAM 3.00 CM.

REQUESTED RESIDUAL RANGE 1.99 CM.

WATER COLUMN SETTING 1.01 CM.

TREATMENT TIME 4.29 MIN.

DOSE (cGy) PRESCRIBED AT ISO-CENTER....	5092.0	
IC2 DOSE (cGy) AT ISO-CENTER	5095.5	100.1 %
IC1 DOSE (cGy) AT ISO-CENTER	5116.8	100.5 %
DOSE (cGy) VARIANCE AT ISO-CENTER (+/-)	35.5	

OPERATOR COMMENTS: 56 GYE 14 NA BEAM CURRENT

DONE BY: IKD

56GYE

NEW ICFs	(C O U N T S / R A D)			
	10-JAN-16	AT	05:22:23	
WC	SEM		IC1SUM	IC2SUM
0.00	12.789		603.356	403.295

OLD ICFs	(C O U N T S / R A D)			
	10-JUN-16	AT	12:22:23	
WC	SEM		IC1SUM	IC2SUM
0.00	12.789		603.356	403.295

NEW/OLD AVG.	1.000	1.000	1.000
--------------	-------	-------	-------

PCFs	(C O U N T S / R A D)			
	10-JUN-16	AT	12:22:23	
WC	SEM		IC1SUM	IC2SUM
1.01	23.379		1119.365	954.334

WATER				
COLUMN		SEM	IC1SUM	IC2SUM
VALUE		COUNTS	COUNTS	COUNTS
1.01	EXP	119045.617	5699806.500	4859467.000
1.01	REC	116685.289	5727565.000	4862787.000

FET6

PATIENT TREATMENT SUMMARY SHEET

LF: [225,251]E169997S1.011

PATIENT NAME: STEFANIE EXPT
PATIENT I.D.: E169997S1.011

DATE: 10-JUN-16
TIME: 13:12:26

SPREAD BRAGG PEAK WIDTH 2.00 CM.
AVAILABLE RANGE OF BEAM 3.00 CM.
REQUESTED RESIDUAL RANGE 1.99 CM.
WATER COLUMN SETTING 1.01 CM.
TREATMENT TIME 8.46 MIN.

DOSE (cGy) PRESCRIBED AT ISO-CENTER.... 10184.0
IC2 DOSE (cGy) AT ISO-CENTER 10186.4 100.0 %
IC1 DOSE (cGy) AT ISO-CENTER 10248.9 100.6 %
DOSE (cGy) VARIANCE AT ISO-CENTER (+/-) 102.2

OPERATOR COMMENTS: 112 gYe

DONE BY: IKD

112 GYE

NEW ICFs (COUNTS / RAD)
10-JAN-16 AT 05:22:23
WC SEM IC1SUM IC2SUM
0.00 12.789 603.356 403.295

OLD ICFs (COUNTS / RAD)
10-JUN-16 AT 12:22:23
WC SEM IC1SUM IC2SUM
0.00 12.789 603.356 403.295

NEW/OLD AVG. 1.000 1.000 1.000

PCFs (COUNTS / RAD)
10-JUN-16 AT 12:22:23
WC SEM IC1SUM IC2SUM
1.01 23.379 1119.365 954.334

WATER COLUMN VALUE SEM COUNTS IC1SUM COUNTS IC2SUM COUNTS
1.01 EXP 238091.23411399613.000 9718934.000
1.01 REC 231132.81311472306.000 9721215.000

SEM

no. of Particles
IC2

0-JUN-16 12:10:00
1.01
23.37895 1119.36499

PATIENT DOSIMETRY
WATER COLUMN SETTING (CM.)
954.33362 MONITOR UNITS / cGy

-1.0
10-JUN-16 12:22:23
3.00
0.00
12.78860 603.35571

DAILY DOSIMETRY
MEASURED RANGE OF BEAM (CM.)
WATER COLUMN SETTING (CM.)
403.29504 MONITOR UNITS / cGy

SERIAL # OF EGG CHAMBER USED FOR CALIBRATION: FW 95-TG

NAME OF THIS FILE IS: LF:[225,265]E169997S1.011

RP = 1.99
SOBP = 2.0

only = 1.0

2nd 11.73

4
4
2
1.0

B.ID.01.AS.005 E169997S1.011
 TB.ID.01.AS.001 STEFANIE EXPT
 TB.ID.01.NM.001 1
 TB.ID.01.NM.004 01
 TB.CL.05.DX.002 25.
 TB.CL.05.DX.003 25.
 TB.RR.01.DX.001 2.0
 TB.HI.05.DX.002 1.99
 TB.BC.01.NM.001 1273.0000
 TB.LG.01.AS.007 E169997S1.011
 TB.ID.01.AS.003 IKD
 TB.CK.01.AS.001 12:07:15
 TB.CK.01.AS.002 10-JAN-16
 ; DOSIMETRY EXPERIMENT

;PATIENT ID
 ;PATIENT NAME
 ;VERSION NUMBER
 ;PORT NUMBER
 ;APERTURE WIDTH (MM)
 ;APERTURE LENGTH (MM)
 ;SPREAD-BRAGG-PEAK WIDTH (CM)
 ;REQUESTED RESIDUAL RANGE (CM)
 ;PHYSICAL DOSE (cGy)
 ;LOGGING FILE NAME
 ;PHYSICIST NAME
 ;TIME PRESCRIPTION WRITTEN
 ;DATE PRESCRIPTION WRITTEN

$$RR = 1.99$$

$$SOBP = 2.0$$

$$poly = 1.0$$

2mm 1273

$$\begin{array}{r}
 4 \\
 4 \\
 2 \\
 \hline
 1.0
 \end{array}$$

Appendix B

Experimental Code

B.1 Data Capture - Ids vs. Vgs

```
1 % Author - Stefanie Garcia
2           % UC Berkeley, Maharbiz Lab
3
4 %% Instructions:
5
6 % 1. Connect Arduino.
7
8 % 2. Write i2c
9
10 % (2.5 Optional) - run read and write checks to ensure MATLAB communication
11 % is working properly.
12     % Can check drain and gate iteration, as well as V_out.
13     % When device is off, make sure all V_out voltages are read into MATLAB
14     % as ZERO.
15
16 % 3. Run Data Collection Code. Code for both the ALD1106 nMOS and the
17 % Maharbiz Lab ASIC is included
18
19 % 4. Plot IV Curves
20 %-----%
21
22 %% Connect Arduino
```

```

23
24 % if doesnt work: go to terminal
25 % ls /dev*/
26 % current address: tty.usbmodem1411
27 % tty.usbmodem14241
28
29 clear all
30
31 a = arduino('/dev/tty.usbmodem1411','Uno')
32 %-----%
33
34 %% Write i2cdev
35
36 dev1 = i2cdev(a, '0x2C','bus',0) %Drain Voltage - % 01011 00 - drain on ...
    breadboard, gate on PCB
37 dev2 = i2cdev(a, '0x2F','bus',0) %Gate Voltage - % 01011 11 - gate on ...
    breadboard, drain on PCB
38 %-----%
39
40 %% read and write checks
41 writeRegister(dev1,hex2dec('0'), 0) %Drain Voltage
42 pause(0.1)
43 readVoltage(a,1)
44
45
46 writeRegister(dev2,hex2dec('0'), 0) %Gate Voltage
47 pause(0.1)
48 readVoltage(a,0)
49
50 readVoltage(a,2)
51 %-----%
52
53 %% iterate drain checks:
54
55 tic
56
57 step = 1;
58
59 for i = 1:255
60     writeRegister(dev1,hex2dec('0'), i*step) %Drain Voltage

```

```

61     pause(0.01)
62     A0_drain_after_amp(i) = readVoltage(a,1);
63     pause(0.01)
64 end
65
66 writeRegister(dev1,hex2dec('0'), 0)
67 pause(0.1)
68 readVoltage(a,1)
69
70 t = toc
71 %-----%
72
73 %% iterate gate checks:
74
75 tic
76
77 step = 51;
78
79 for i = 1:5
80     writeRegister(dev2,hex2dec('0'), i*step) %Gate Voltage - up to 5V from ...
81         arduino
82     pause(0.1)
83     A1_gate_afterR(i) = readVoltage(a,0)
84     pause(1)
85 end
86 writeRegister(dev2,hex2dec('0'), 0)
87 pause(0.1)
88 readVoltage(a,0)
89
90 t = toc
91 %-----%
92
93 %% V_out checks
94
95 writeRegister(dev1,hex2dec('0'), 0) %Drain Voltage - up to 5V from arduino
96 writeRegister(dev2,hex2dec('0'), 0) %Gate Voltage - up to 5V from arduino
97
98 readVoltage(a,1) % Vds
99 readVoltage(a,0) % Vgs

```

```

100
101 readVoltage(a,2) %V_out
102 %-----%
103
104 %% *** Data Collection *** Ids vs Vgs for ALD1106
105
106     time1 = 0.01;
107     timefix= 0.1;
108
109 writeRegister(dev1,hex2dec('0'), 0) %drain
110 pause(time1)
111 initial_drain = readVoltage(a,1)
112 pause(time1)
113
114 writeRegister(dev2,hex2dec('0'), 0) %gate
115 pause(time1)
116 initial_gate = readVoltage(a,0)
117 pause(time1)
118
119 initial_V_out = readVoltage(a,2)
120 pause(time1)
121
122 % at Vds = 0 V:
123
124 writeRegister(dev2,hex2dec('0'), 0) %Gate Voltage - 0 to 5V
125 pause(time1)
126 A0_gate0 = readVoltage(a,0);
127 pause(time1)
128
129     step_drain = 51;
130
131     for j = 1:5
132         writeRegister(dev1,hex2dec('0'), j*step_drain) %Drain Voltage ...
            - 0 to 5V
133         pause(time1)
134         A1_drain0(j) = readVoltage(a,1);
135         pause(time1)
136         V_out0(j) = readVoltage(a,2);
137         pause(time1)
138     end

```

```

139
140
141 % at Vds = 1, 2, 3, 4, 5 V
142
143 tic
144
145 step_drain = 51;
146
147 for i = 1:5
148     writeRegister(dev1,hex2dec('0'), i*step_drain) %Drain Voltage - 0 to 5V
149     pause(time1)
150     A1_drain(i) = readVoltage(a,1);
151     pause(time1)
152
153     step_gate = 1;
154
155     for j = 1:255
156         writeRegister(dev2,hex2dec('0'), j*step_gate) %Gate Voltage - ...
157             0 to 5V
158         pause(time1)
159         A0_gate(i,j) = readVoltage(a,0);
160         pause(time1)
161         V_out(i,j) = readVoltage(a,2);
162         pause(time1)
163     end
164 end
165
166
167 writeRegister(dev1,hex2dec('0'), 0)
168 pause(timefix)
169 readVoltage(a,1)
170 pause(timefix)
171
172 writeRegister(dev2,hex2dec('0'), 0)
173 pause(timefix)
174 readVoltage(a,0)
175 pause(timefix)
176
177 t=toc

```

```

178 %-----%
179
180 %% *** Data Collection *** Ids vs Vgs for Maharbiz Lab ASIC
181
182     timel = 0.01;
183     timefix= 0.1;
184
185 writeRegister(dev1,hex2dec('0'), 0) %drain
186 pause(timel)
187 initial_drain = readVoltage(a,1)
188 pause(timel)
189
190 writeRegister(dev2,hex2dec('0'), 0) %gate
191 pause(timel)
192 initial_gate = readVoltage(a,0)
193 pause(timel)
194
195 initial_V_out = readVoltage(a,2)
196 pause(timel)
197
198 % at Vgs = 0 V:
199
200 writeRegister(dev2,hex2dec('0'), 0) %Gate Voltage - 0 to 0.8V
201 pause(timel)
202 A0_gate0 = readVoltage(a,0);
203 pause(timel)
204
205     step_drain = 51;
206
207     for j = 1:5
208         writeRegister(dev1,hex2dec('0'), j*step_drain) %Drain Voltage ...
                - 0 to 1V
209         pause(timel)
210         A1_drain0(j) = readVoltage(a,1);
211         pause(timel)
212         V_out0(j) = readVoltage(a,2);
213         pause(timel)
214     end
215
216

```

```

217 % at Vds = 1, 2, 3, 4, 5 V
218
219 tic
220
221 step_drain = 10;
222
223 for i = 1:5
224     writeRegister(dev1,hex2dec('0'), i*step_drain) %Drain Voltage - 0 to 1V
225     pause(time1)
226     A1_drain(i) = readVoltage(a,1);
227     pause(time1)
228
229     step_gate = 1;
230
231     for j = 1:41
232         writeRegister(dev2,hex2dec('0'), j*step_gate) %Gate Voltage - ...
                0 to 0.8V
233         pause(time1)
234         A0_gate(i,j) = readVoltage(a,0);
235         pause(time1)
236         V_out(i,j) = readVoltage(a,2);
237         pause(time1)
238     end
239
240 end
241
242
243 writeRegister(dev1,hex2dec('0'), 0)
244 pause(timefix)
245 readVoltage(a,1)
246 pause(timefix)
247
248 writeRegister(dev2,hex2dec('0'), 0)
249 pause(timefix)
250 readVoltage(a,0)
251 pause(timefix)
252
253 t=toc
254 %-----%
255

```

```

256 %% Plot Ids vs Vgs
257
258 i_ds = V_out/330; % i_ds is 5x255 double
259 %i_ds0 = V_out0/330;
260
261 %plot(A0_gate0, i_ds0, 'k.')
262
263 hold on
264 grid on
265
266 plot(A0_gate(1,:), i_ds(1,:), 'r.')
267 plot(A0_gate(2,:), i_ds(2,:), 'g.')
268 plot(A0_gate(3,:), i_ds(3,:), 'c.')
269 plot(A0_gate(4,:), i_ds(4,:), 'b.')
270 plot(A0_gate(5,:), i_ds(5,:), 'm.')
271
272     xlabel('V gs [V]')
273     ylabel('I ds [A]')
274     title('xxxxxxx')
275     legend(sprintf('V ds = %0.3f V', A1_drain(1,1)), sprintf('V ds = ...
        %0.3f V', A1_drain(1,2)), sprintf('V ds = %0.3f V', ...
        A1_drain(1,3)), sprintf('V ds = %0.3f V', A1_drain(1,4)), ...
        sprintf('V ds = %0.3f V', A1_drain(1,5)))
276
277     hold off

```

B.2 Data Capture - Ids vs. Vds

```
1 % Author - Stefanie Garcia
2           % UC Berkeley, Maharbiz Lab
3
4 %% Instructions:
5
6 % 1. Connect Arduino.
7
8 % 2. Write i2c
9
10 % (2.5 Optional, Code in the VGS VS IDS section) - run read and write ...
    checks to ensure MATLAB communication
11 % is working properly.
12     % Can check drain and gate iteration, as well as V_out.
13     % When device is off, make sure all V_out voltages are read into MATLAB
14     % as ZERO
15
16 % 3. Run Data Collection Code. Code for both the ALD1106 nMOS and the
17 % Maharbiz Lab ASIC is included
18
19 % 4. Plot IV Curves
20 %-----%
21
22 %% Connect Arduino
23
24 % if doesnt work: go to terminal (on a mac)
25 % ls /dev*/
26 % current address: tty.usbmodem1411
27 % Other address that might work -> tty.usbmodem14241
28
29 clear all
30
31 a=arduino('/dev/tty.usbmodem1411','Uno')
32 %-----%
33
34 %% Write i2c
35
```

```

36 dev1 = i2cdev(a, '0x2C', 'bus', 0) %Drain Voltage - % 01011 00 - A1
37 dev2 = i2cdev(a, '0x2F', 'bus', 0) %Gate Voltage - % 01011 11 - A0
38 %-----%
39
40 %% *** Data Collection *** Ids vs Vds for ALD1106
41
42     time1 = 0.01;
43     timefix= 0.1;
44
45 writeRegister(dev1,hex2dec('0'), 0) %drain
46 pause(time1)
47 initial_drain = readVoltage(a,1)
48 pause(time1)
49
50 writeRegister(dev2,hex2dec('0'), 0) %gate
51 pause(time1)
52 initial_gate = readVoltage(a,0)
53 pause(time1)
54
55 initial_V_out = readVoltage(a,2)
56 pause(time1)
57
58 tic
59
60 % at Vgs = 0V:
61
62 writeRegister(dev2,hex2dec('0'), 0) %Gate Voltage - 0 to 5V
63 pause(time1)
64 A0_gate0 = readVoltage(a,0);
65 pause(time1)
66
67     step_drain = 1;
68
69     for j = 1:255
70         writeRegister(dev1,hex2dec('0'), j*step_drain) %Drain Voltage ...
71             - 0 to 5V
72         pause(time1)
73         A1_drain0(j) = readVoltage(a,1);
74         pause(time1)
75         V_out0(j) = readVoltage(a,2);

```

```

75         pause(time1)
76     end
77 %}
78
79 % at Vgs = 1, 2, 3, 4, 5
80
81 t1 = toc
82
83 step_gate = 51;
84
85 for i = 1:5
86     writeRegister(dev2,hex2dec('0'), i*step_gate) %Gate Voltage - 0 to 5V
87     pause(time1)
88     A0_gate(i) = readVoltage(a,0);
89     pause(time1)
90
91     step_drain = 1;
92
93     for j = 1:255
94         writeRegister(dev1,hex2dec('0'), j*step_drain) %Drain Voltage ...
95             - 0 to 5V
96         pause(time1)
97         A1_drain(i,j) = readVoltage(a,1);
98         pause(time1)
99         V_out(i,j) = readVoltage(a,2);
100        pause(time1)
101    end
102 end
103
104
105 writeRegister(dev1,hex2dec('0'), 0)
106 pause(timefix)
107 readVoltage(a,1)
108 pause(timefix)
109
110 writeRegister(dev2,hex2dec('0'), 0)
111 pause(timefix)
112 readVoltage(a,0)
113 pause(timefix)

```

```

114
115 t2 = toc
116 %-----%
117
118 %% *** Data Collection *** Ids vs Vds for Maharbiz Lab ASIC
119
120     time1 = 0.01;
121     timefix= 0.1;
122
123 writeRegister(dev1,hex2dec('0'), 0) %drain
124 pause(time1)
125 initial_drain = readVoltage(a,1)
126 pause(time1)
127
128 writeRegister(dev2,hex2dec('0'), 0) %gate
129 pause(time1)
130 initial_gate = readVoltage(a,0)
131 pause(time1)
132
133 initial_V_out = readVoltage(a,2)
134 pause(time1)
135
136 tic
137
138 % at zero:
139
140 writeRegister(dev2,hex2dec('0'), 0) %Gate Voltage - 0 to 0.8V
141 pause(time1)
142 A0_gate0 = readVoltage(a,0);
143 pause(time1)
144
145     step_drain = 1;
146
147     for j = 1:51
148         writeRegister(dev1,hex2dec('0'), j*step_drain) %Drain Voltage ...
149             - 0 to 1V
150         pause(time1)
151         A1_drain0(j) = readVoltage(a,1);
152         pause(time1)
153         V_out0(j) = readVoltage(a,2);

```

```

153         pause(time1)
154     end
155
156 % at Vgs = 1, 2, 3, 4, 5
157 t1 = toc
158
159 step_gate = 10;
160
161 for i = 1:4
162     writeRegister(dev2,hex2dec('0'), i*step_gate) %Gate Voltage - 0 to 0.8V
163     pause(time1)
164     A0_gate(i) = readVoltage(a,0);
165     pause(time1)
166
167     step_drain = 1;
168
169     for j = 1:51
170         writeRegister(dev1,hex2dec('0'), j*step_drain) %Drain Voltage ...
171             - 0 to 1V
172         pause(time1)
173         A1_drain(i,j) = readVoltage(a,1);
174         pause(time1)
175         V_out(i,j) = readVoltage(a,2);
176         pause(time1)
177     end
178 end
179
180 % try averaging for a few seconds to reduce noise
181 % sample every 100 us, for 100 ms
182
183 %take one without the SOBP
184
185 writeRegister(dev1,hex2dec('0'), 0)
186 pause(timefix)
187 readVoltage(a,1)
188 pause(timefix)
189
190 writeRegister(dev2,hex2dec('0'), 0)
191 pause(timefix)

```

```

192 readVoltage(a,0)
193 pause(timefix)
194
195 t2 = toc
196 %-----%
197
198 %% Plot Ids vs Vds
199
200 i_ds = V_out/330;
201 %i_ds0 = V_out0/330;
202
203 %plot(A1_drain0, i_ds0, 'k.')
204
205 hold on
206 grid on
207
208 plot(A1_drain(1,:), i_ds(1,:), 'm.')
209 plot(A1_drain(2,:), i_ds(2,:), 'r.')
210 plot(A1_drain(3,:), i_ds(3,:), 'g.')
211 plot(A1_drain(4,:), i_ds(4,:), 'c.')
212 plot(A1_drain(5,:), i_ds(5,:), 'b.')
213
214     xlabel('V ds [V]')
215     ylabel('I ds [mA]')
216     title('xxxxxxxx')
217     legend(sprintf('V gs = %0.3f V', A0_gate(1,1)), sprintf('V gs = ...
        %0.3f V', A0_gate(1,2)), sprintf('V gs = %0.3f V', ...
        A0_gate(1,3)), sprintf('V gs = %0.3f V', A0_gate(1,4)), ...
        sprintf('V gs = %0.3f V', A0_gate(1,5)))
218
219     hold off

```

B.3 US Backscatter Integration

```
1 % Author - Stefanie Garcia
2           % UC Berkeley, Maharbiz Lab
3
4 %% Instructions:
5
6 % 1. Load in the .csv scope data.
7     %Load the larger amplitude pulse first, "when Vgs = 0V = off".
8     %Load the smaller amplitude pulse second, "when Vgs = x volts = on".
9
10 % 2. Plot your raw data and look for the window where the PZT piezo region
11 % lies (where there is an amplitude shift)
12
13 % 3. Run Integration Code
14
15 %% Raw Data Plots
16
17 plot(second1,Volt,'b'); %off
18 grid on;
19 hold on;
20 plot(second2, Volt1, 'r') %on
21     xlabel('Time [s]')
22     ylabel('Volts [V]')
23     title('Raw Ultrasound Backscatter Data - xx Gy Irradiation')
24     legend('V gs = 0 V', 'V gs = 5V')
25
26     hold on
27
28 %-----%
29
30 %% Setting window (t = 2.4 - 3.2 in this case):
31
32 % Note: Window will change for each new experiment
33 % data (second1, Volt; and second2, Volt1) is cut to size after visual
34 % inspection of window.
35
36 second1_window = second1(1000:1800);
```

```

37 Volt1_window = Volt(1000:1800);
38 second2_window = second2(1000:1800);
39 Volt2_window = Volt1(1000:1800);
40
41 limits = [2.4*10^-5, 3.2*10^-5, -1.5, 2]; %window for t = 2.4*10^-5 to ...
      3.2*10^-5 region of interest
42
43 plot(second1_window,Volt1_window,'b'); %off
44 grid on;
45 hold on;
46 plot(second2_window, Volt2_window, 'r') %on
47     xlabel('Time [s]')
48     ylabel('Volts [V]')
49     title('Raw Ultrasound Backscatter Data Cropped - 0 Gy Irradiation')
50     legend('V gs = 0 V','V gs = 5V')
51     axis(limits)
52
53     hold on
54 %-----%
55
56 %% Plot - Checking the windowed amplitude shift:
57
58 plot(second1,Volt_P,'b');
59 grid on;
60 hold on;
61 plot(second2, Volt1_P, 'r')
62     xlabel('Time [s]')
63     ylabel('Volts [V]')
64     title('Absolute Value of Raw Data - xx Gy Irradiation')
65     legend('V gs = 0 V','V gs = 5 V')
66
67     hold on
68 %-----%
69
70 %% Windowing and Integration Calculation
71
72 Volt_off_C_P = abs(Volt_off_C);
73 Volt_on_C_P = abs(Volt_on_C);
74
75 [M_off,I_max_off] = max(Volt_off_C_P);

```

```

76 [M_on, I_max_on] = max(Volt_on_C_P);
77
78 window1 = 0.5*10^-6; %set the left hand window
79 window2 = 1.4*10^-6; %set the right hand window
80
81 %-----%
82 % OFF Voltage = 0V Integration:
83
84     % window around that maximum:
85     % try window size: 0.2e-06
86
87     max_S_off = second_off_C(I_max_off);
88     time1 = max_S_off - window1;
89     time2 = max_S_off + window2;
90
91     time1_I = find(second_off_C < time1);
92     time2_I = find(second_off_C > time2);
93
94     % remove from voltage signal
95
96     [a, ~] = size(time1_I);
97     b = time2_I(1);
98
99     Volt_off_C_fix = Volt_off_C_P(a:b);
100    second_off_C_fix = second_off_C(a:b);
101
102    % plot checks
103    % plot(second_off_fix, Volt_off_fix, 'g')
104
105    Area_off_C_P = trapz(second_off_C_fix, Volt_off_C_fix);
106
107 %-----%
108 % ON Voltage = 5V Integration:
109
110     % window around that maximum:
111     % try window size: 0.2e-06
112
113     max_S_on = second_on_C(I_max_on);
114     time3 = max_S_on - window1;
115     time4 = max_S_on + window2;

```

```

116
117     time3_I = find(second_on_C < time3);
118     time4_I = find(second_on_C > time4);
119
120     % remove from voltage signal
121
122     [c,~] = size(time3_I);
123     d = time4_I(1);
124
125     Volt_on_C_fix = Volt_on_C_P(c:d);
126     second_on_C_fix = second_on_C(c:d);
127
128     % Plot for checks
129     % plot(second_off_fix,Volt_off_fix, 'g')
130
131     Area_on_C_P = trapz(second_on_C_fix, Volt_on_C_fix);
132
133     %-----%
134     % PERCENTAGE CALCULATIONS
135
136     percent_shrink = 100*(Area_on_C_P/Area_off_C_P);
137
138     percent_shift_in_amplitude = 100 - (100*(Area_on_C_P/Area_off_C_P));
139
140     %-----%

```